UNIVERSITÀ DEGLI STUDI
DI GENOVA

UNIVERSITA' DEGLI STUDI DI GENOVA
Facoltà di Fisica

ISTITUTO ITALIANO DI TECNOLOGIA
Quantum Materials Theory

TOWARDS TOPOLOGICAL SWITCHING IN MULTIFERROICS

Author
Alessandro Granero

Supervisors
Sergey Artyukhin
Riccardo Ferrando
Co-supervisors
Niccolò Traverso Ziani

Genova, 2024

Acknowledgments

I sincerely thank, from the bottom of my heart, my entire family and all my friends for always being by my side and for sharing with me both the good times and the not-so-good ones. Thank you, each of you is far more important than you realize. I also deeply thank my supervisor, for giving me the opportunity to work on such interesting topics and for showing me what it means to do research and love one's work.
It would take too many words to explain how thankful I am, so I'll just leave here a few words by Mariangela Gualtieri.

Una nostalgia d'imperfetto
ci gonfierà i fotoni lucenti.
Sii dolce con me.
Maneggiami con cura.
Abbi la cautela dei cristalli
con me e anche con te.

Contents

Università degli studi di Genova

Abstract

Dipartimento di Fisica (DIFI)
Quantum Materials Theory, IIT

Master Degree Thesis

Towards topological switching in multiferroics

Magnetoelectric switching in $GdMn_2O_5$ is the first known topological ferroic switching phenomenon where sweeping the magnetic field across the spin reorientation transition leads to incremental 90 degrees rotations of spins, with a spin winding number acting as a topological invariant. Here we aim to elucidate the underlying mechanism of this behavior in terms of symmetry requirements and the ingredients of the model Hamiltonian that enable the behavior, with the goal of identifying other materials and topological switching phenomena. Such endeavors not only deepen our understanding of these phenomena but also pave the way for potential applications in computing and storage technologies.

In a basic model of conventional ferroelectric switching, the free energy has two minima corresponding to domains with polarization $+P$ and $-P$. External electric field E lowers one of the minima, but the barrier between them persists, and switching is facilitated by nucleation of domains with favored polarization and domain wall motion. In contrast, in topological switching, external field sweeps drive the evolution of the potential energy landscape so that the energy minimum moves in the space of spin orientations, with the bulk spin configuration continuously morphing between zero-field states.

The approach involves constructing Landau free energy, based on the symmetry, starting from the simplest case of two antiferromagnetic spin chains interacting with external magnetic and electric fields. Here we establish the basic toy model that elucidates how symmetry of the system and specific spin interactions enable topological switching. This is followed by numerical simulations to corroborate recent experimental observations of electric field controlled switching. We hope the results will provide a fertile ground for future research aimed at unravelling the full extent of these intriguing phenomena.

Chapter 1

Introduction

1.1 Motivation: magnetic memory, data writing and read-out

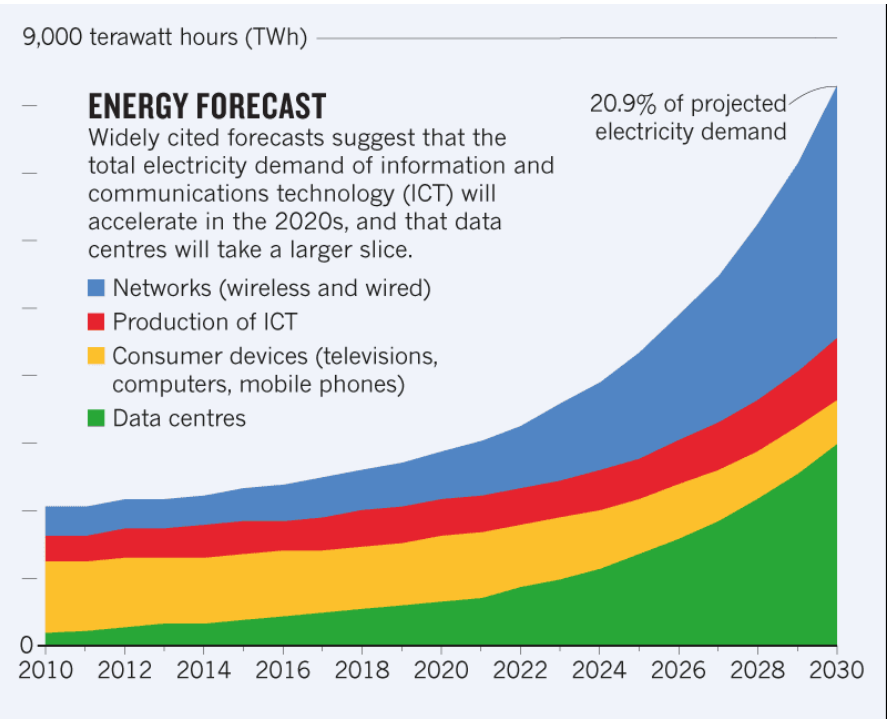

FIGURE 1.1: "Bits are so "tiny" and weightless we often disregard their impact on energy. The he problem is that the amount of bits is staggering and the equipment needed to manage them is very power intensive. The graphic shows the expected increase in power usage in this decade to manage "bits". As you can see the lion share is taken by networks and by data centres." Adopted from Clarissa Garcia, AKCP Industrial Metaverse – Sustainability.

The ongoing digital transformation has heralded a new era where data is as critical a resource as electricity was during the industrial revolution. This transformation is heavily reliant on the complex ecosystem of information and communications technology (ICT), encompassing data centers, networks, and consumer devices. As depicted in the energy forecast, the ICT sector's electricity demands are projected to surge dramatically by 2030, constituting a significant proportion of global energy consumption.

Data centers are the backbone of the digital age, providing the infrastructure necessary for cloud computing, data processing, and storage. As digital services expand—from streaming platforms to sophisticated AI computations—the capacity and number of data centers are increasing. This expansion translates to a corresponding rise in electricity demand. Data centers are energy-intensive, primarily due to the considerable amount of power required for computing operations and cooling systems. Innovations in energy efficiency, such as advanced thermal management and renewable energy adoption, are being explored to reduce this footprint.

On the consumer end, devices like smartphones, computers, and IoT gadgets continuously demand higher energy capacity to support advanced functionalities. While individual devices may have relatively low power consumption, the aggregate effect is substantial.

FIGURE 1.2: (left) Google Data Center Campus near Portland, Oregon. (right) Interior view of a data center.

1.1.1 Traditional magnetic memories and ferroic switching

Magnetic memories, including Magnetic Random-Access Memory (MRAM) and Spin-Transfer Torque MRAM (STT-MRAM), are increasingly pivotal in managing the data deluge due to their scalability, non-volatility, and speed. However, their operation is energy-intensive, largely due to the physics underpinning magnetic data storage and retrieval processes [Bader, 2006; Bibes and Barthélémy, 2008]. Magnetic memories operate by manipulating magnetic domains within materials. Data writing involves moving these domain walls—a process known as ferroic switching. When a magnetic field is applied, the domain walls shift, expanding the domains with spins aligned to the

field orientation, that represent stored data. This movement requires energy, leading to energy dissipation, equal to the hysteresis loop area.

Hysteresis is a critical factor contributing to energy loss in magnetic memories. It describes the lag between the applied magnetic field and the resultant magnetization. The hysteresis loop area defines the energy wasted as heat during each magnetic cycle. Reducing hysteresis through material engineering can mitigate some energy losses, but often at the expense of other performance attributes.

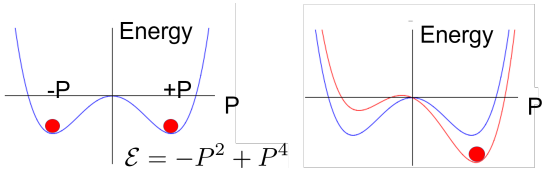

(A) Switching through propagation of domain wall

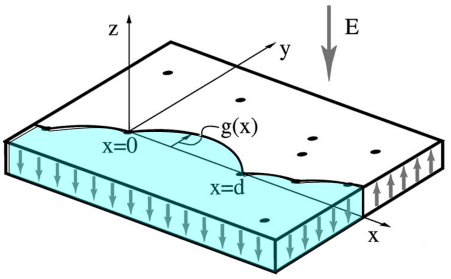

(B) Nucleation of domain wall

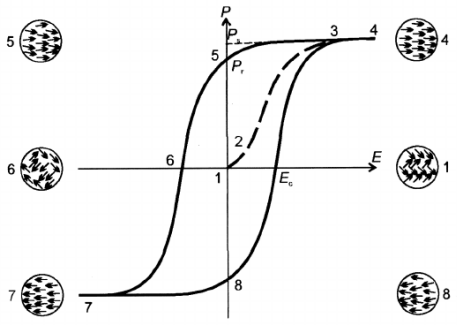

(C) Example of hysterisis loop

Hence, the urgency of a groundbreaking innovation in the field of magnetic memories and data storage arises naturally as one of the few possible ways that we as humankind have to help mitigate the environmental impact while meeting the needs of the digital future.

The present work hopes to be a modest contribution to a bigger picture that could pave the way to such innovative technologies, in addition to providing insights into the physics of a phenomenon that is still not well understood, describing and trying to comprehend the impactful mechanism of the topologically protected magnetoelectric switching taking place in $GdMn_2O_5$.

1.2 Landau theory for ferroic orders and switching

When it comes to phase transition in condensed matter, Landau Theory is a game changer theory that enables deep yet simple analytical description of the considered

system. It is therefore necessary to introduce this theory to understand how it works and how we took advantage of it in building a powerful model for our system, which helps us to understand its unique behaviour.

1.2.1 Phase transitions

First of all, let's clarify what is interpreted as a phase transition. Generally speaking, phase transitions are ubiquitous in nature, and they occur when the equilibrium state of a system changes qualitatively as a function of externally imposed stimuli. These stimuli could be changes in temperature, pressure, magnetic field, concentration, degree of crosslinking, or any number of other physical quantities. So, phase transitions define the state of the matter we are dealing with. Then, it is obvious that both predicting their existence and also understanding their character is fundamental for technology and plays one of the main roles in statistical and condensed matter physics.

Among the several different types of phase transitions, let's focus now on the kind of our interest: the magnetic phase transitions. Starting from a general case, a material that exhibits a long-range magnetic ordering at low temperatures and in zero magnetic field is characterized by at least two phases: the high temperature paramagnetic phase and the magnetically ordered ground-state phase. What establishes the ground-state phase, at least in simple systems, is the magnetic-ordering temperature, that is the critical temperature at which a material undergoes a transition from a disordered magnetic state to an ordered one. This temperature is critical because it marks the point where thermal energy becomes comparable to the energy associated with magnetic interactions, causing a change in the material's magnetic properties. It can be defined according to two main types: the Curie temperature (or Curie point), T_C, that is the temperature above which a material loses their ferromagnetic long range order (which can be usually replaced by induced magnetism), or the Néel temperature, T_N, that is the temperature above which an antiferromagnetic material becomes paramagnetic, namely where the antiferromagnetic long-range ordering of spins is destroyed. In some cases then, the ground-state phase is immediately below this magnetic ordering temperature (T_C or T_N). Frequently, the magnetically-ordered phase, that appears below this temperature, is different from the ground-state phase. Thus, one or more magnetic phase transitions are observed at temperatures below T_C (or T_N).

When an external magnetic field is applied, new magnetic phases may appear, that are usually called metamagnetic, and the related magnetic phase transitions (with respect to the external magnetic field as a control parameter) are called metamagnetic transitions. There are two types of phase transitions between two magnetic phases: first-order and

second-order transitions. They can be distinguished by a discontinuity of the first derivative (e.g. the magnetization, for 1st order) or of the second derivative (e.g. the magnetic susceptibility, for the second order) of the magnetic part of the free energy. These transitions are usually reflected in real materials in the changes of transport, thermodynamic and other material properties.

A powerful and schematic tool useful in this discussion is the magnetic phase diagram, which shows the different phases adopted by a material over a range of varying parameters. Usually temperature T, external magnetic field H, and sometimes external pressure P or a concentration of a substituting element x, are the parameters used in these representations. In the cases of our interest, the used one is the $H - T$ diagram. Magnetic phase diagrams of simple magnetic systems can contain only two phases: the paramagnetic phase and one magnetically ordered phase. When it comes to more complex materials with competing interactions, the phase diagram becomes rather rich and presents multiple nontrivial phases. In strongly anisotropic magnetic systems a complete description requires up to three different magnetic phase diagrams, one each for the magnetic fields applied along the three principal crystallographic directions.

1.2.2 Landau theory

The background just discussed, that is phase transitions combined with the finite group symmetry breaking, forms the framework for the widely applicable approach provided by the Landau theory of phase transitions. Indeed, different states of condensed matter are characterized by different quantities: density, crystal symmetry, magnetization, electric polarization and a lot more. Many such states can have a certain order, and different types of ordering can be characterized by order parameters. In Landau theory, order parameter (that is a finite dimensional variable) describes the degree of order and symmetry breaking, and symmetry-related domains with different directions of order parameter correspond to minima of the Landau potential. Some examples of order parameters are the magnetization for ferromagnets, the electric polarization for ferroelectrics, and a condensate wave function for superconductivity. Naturally, the higher the temperature, the more disordered is the system, hence certain types of ordering arise on lowering the temperature. Just think about basic thermodynamics, where the state of the system, at a finite temperature, is chosen by the condition of the minimum of the corresponding thermodynamic potential, such as the Helmholtz free energy

$$F = E - TS = -T \ln Z, \tag{1.1}$$

or the Gibbs free energy

$$\Phi(P,T) = E - TS + PV = F + PV, \tag{1.2}$$

where T is the temperature, S is the entropy, $S = \ln Z + \frac{E}{T}$, E is the average energy of the system, $E = \frac{1}{Z}\sum_n E_n e^{-E_n/T}$ and Z is the partition function $Z = \sum_n e^{-E_n/T}$. From these functions, one can clearly see that increasing the temperature means favoring states with higher entropy, leading to a more disordered state. It is evident then how the types of order have to be established, in order for the minimum of energy to reach those orderings, below a certain temperature, where entropy is not relevant anymore.

The general order parameter η depends on temperature, as well as on other external parameters. An essential example of temperature-dependence in the order parameter are the first and second -order phase transition. In the former, η changes rapidly in a jump like-fashion, at the critical temperature T_C, while in the latter it changes smoothly and continuously. The critical temperature T_C could often be the already mentioned Curie temperature. They are illustrated in Figure 1.4.

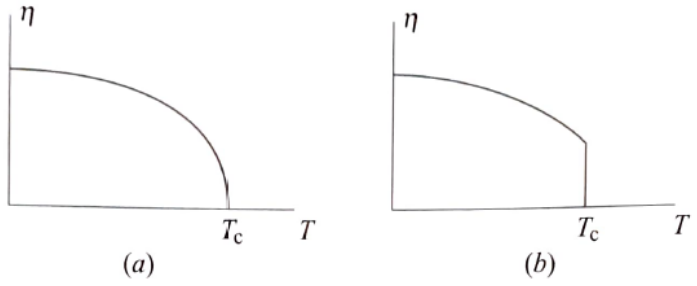

FIGURE 1.4: **Dependence of order parameter η on temperature in phase transitions: a**, Second-order phase transition, η changes continuously. **b**, first-order phase transition, η changes in a jump-like fashion.

1.2.3 Second-order phase transitions

The case of our interest are the second-order phase transitions. Following the procedure by Landau and Lifshits (1980), when the system is close to T_C the order parmeter η is small enough to expand the Gibbs free energy $\Phi(\eta)$ in a Taylor series, since the order parameter must be small near the transition, which results in general in the free energy of the form

$$\Phi = \Phi_0 + \alpha\eta + A\eta^2 + C\eta^3 + B\eta^4 + \dots. \tag{1.3}$$

The condition that determines the state of the system, specifically the order parameter η, is that the free energy must be minimal. As one can clearly see from the expression above, $\Phi(P,T,\eta)$ depends explicitly on η (while the coefficients α, A, B, C, D depend

on P and T), so it is evident that above T_C Φ has its minimum at $\eta = 0$, while for temperature below T_C the minimum corresponds to a (small) $\eta \neq 0$. It naturally follows that, in the absence of an external field, the coefficient α should be $\alpha = 0$, otherwise $\eta \neq 0$ at all temperatures and the linear term in Equation 1.3 makes the free energy never having a minimum at $\eta = 0$ (that could be the case of a disordered system, for $T > T_C$).
These requirements then drive to a condition for the first nonzero term $A\eta^2$ in our expression, that is

$$\begin{aligned} A(P,T) > 0 \quad for \quad T > T_C \\ A(P,T) < 0 \quad for \quad T < T_C \end{aligned} \tag{1.4}$$

Hence, assuming it changes continuously with temperature, the coefficient $A(P,T)$ at $T = T_C$ should pass through zero and change sign, as we can see in Figure 1.5.

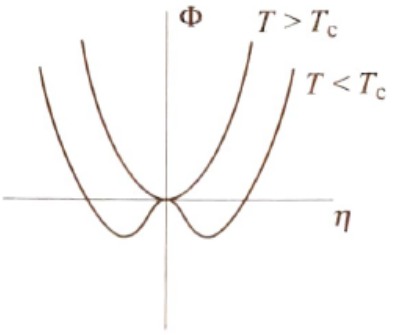

FIGURE 1.5: **Dependence of $\Phi(\eta)$ on** η for temperatures above or below T_C.

About other coefficients in Equation 1.3, is usually assumed to have C=0 and B>0. Also, within the simplest assumption, we chose, close to $T = T_C$,

$$A(P,T) = a(T - T_C) \tag{1.5}$$

with $\alpha > 0$, so that Equation 1.3 becomes

$$\Phi = \Phi_0 + A\eta^2 + B\eta^4 = \Phi_0 + a(T - T_C)\eta^2 + B\eta^4. \tag{1.6}$$

Minimizing this expression of the free energy with respect to η one can found the behaviour of $\eta(T)$:

$$\frac{\partial \Phi}{\partial \eta} \Longrightarrow 2A\eta + 4B\eta^3 = 2a(T - T_C)\eta + 4B\eta^3 = 0 \tag{1.7}$$

$$\eta^2 = -\frac{A}{2B} = \frac{a}{2B}(T - T_C) \tag{1.8}$$

Figure 1.6 displays such behaviour.

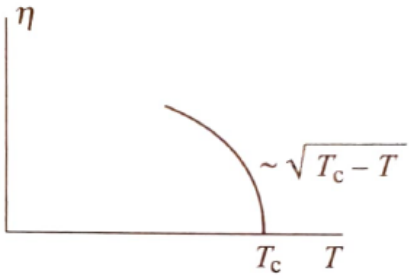

FIGURE 1.6: Behaviour of order parameter η according to Equation 1.8.

We will neglect the possible dependence of the coefficients on other external variables, since usually the most important dependence is $T_C(P)$, while a and B are taken as constants.

Putting the equilibrium value of the order parameter Equation 1.8 back into the free energy in Equation 1.3, one can get the equilibrium free energy at $T < T_C$:

$$\Phi_{min} = \Phi_0 - \frac{A^2}{4B} = \Phi_0 - \frac{a^2}{4B}(T - T_C)^2 \tag{1.9}$$

while for $T > T_C \quad \Phi_{min} = \Phi_0$.

Hence, Φ is continuous, as well as other thermodynamics potentials, like the Helmholtz free energy. However, the derivatives of these free energy with respect to the temperature, $\frac{\partial \Phi}{\partial T}$, have a kinks at T_C, so the second derivative would have jumps, as presented in Figure 1.7, drawing the so called "Lambda function".

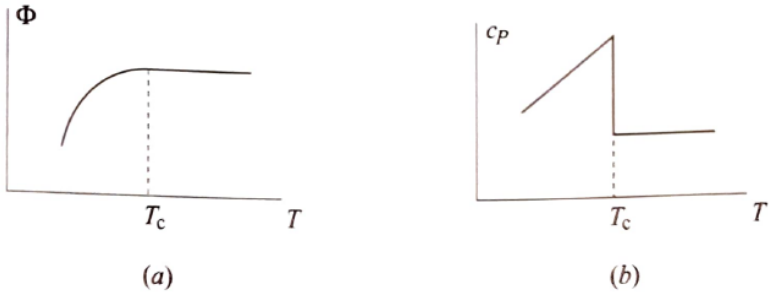

FIGURE 1.7: **a**, Φ (or other thermodynamic potentials) are continuous during a second-order phase transition. **b**, Lambda function: second derivatives jump in a second-order phase transition.

This behaviour is typical for thermodynamic functions at second-order phase transitions in the Landau theory.

1.3 Topological switching

In order to better understand the topological switching that will be presented shortly, it is useful to recall a few fundamental concepts about one of the main topological effect and the idea of quantum pumping. A quantum pump is a device able to generate a particle current via slow and periodic modulation of at least two system parameters, in the absence of any external bias, and one of its maximum expression is achieved in Thouless (or topological) pump: an example of non-equilibrium physics (in the adiabatic regime) where non-trivial topological properties arise as a manifestation of Berry phase in transport.

1.3.1 Thouless pumping

Problem considered by Thouless [Thouless, 1983] is that of a one-dimensional insulator subjected to a time-dependent potential term trying to drive the system in one direction. Its Hamiltonian is

$$\hat{H}(t) = \sum_{j}^{N}(\frac{\hat{p}_j^2}{2m} + V_s(x_j) + V_l(x_j - vt)) + \frac{1}{2}\sum_{i\neq j} V_{int}(|x_i - x_j|) \tag{1.10}$$

where, (accordingly to recent experimental realizations), $V_s(x) = V_s sin^2\left(\frac{\pi x}{d_s} + \frac{\pi}{2}\right)$ is a periodic potential of period d_s (induced by a pair of counter-propagating lasers with a certain wavelength), and similarly V_l is a periodic potential with longer periodicity: $d_s = \frac{1}{2}d_l$:

$$V_l(x - vt) = V_l \sin^2\left(\frac{\pi(x - vt)}{d_l}\right) = V_l \sin^2\left(\frac{\pi x}{d_l} - \frac{\phi(t)}{2}\right) \tag{1.11}$$

where $\phi(t) = 2\pi vt/d_l$. Hamiltonian is clearly time-periodic ($H(t = 0) = H(t = T)$), and also, for any fixed t, the potential is periodic with a lattice constant $a = d_l = 2d_s$.

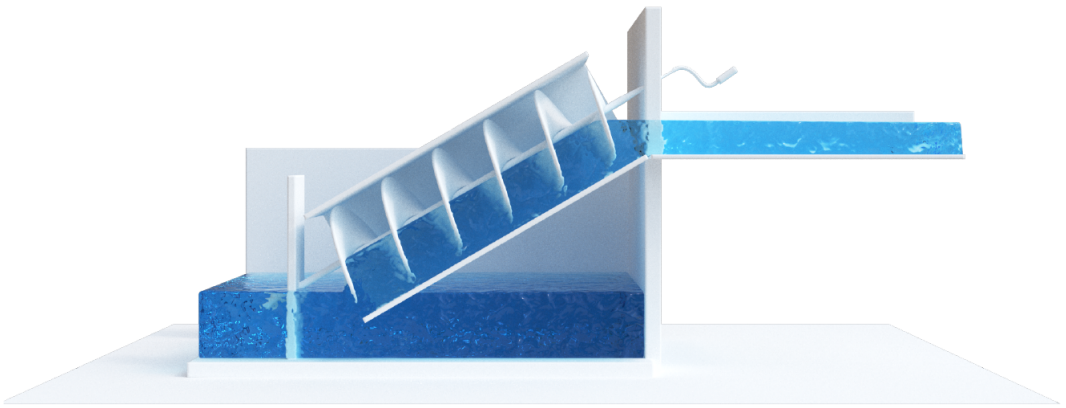

FIGURE 1.8: **Archimede's screw** is a commonly used example to visualize the mechanism of Thouless pumping. The screw pumps a certain amount of water at every (unidirectional) rotation.

Assumption made by Thouless is this system to be an insulator, which usually should mean that, if $\hat{J}_x$ is the total current operator in the x-direction and $|\Psi(0)>$ is the ground state of $\hat{H}(0)$, then $<\Psi(0)|\hat{J}_x|\Psi(0)>=0$. But the ground-breaking discovery by Thouless is that even insultators can in certain cases transport charge, and if one computes the charge transported in a period T,

$$Q = \lim_{L\to\infty} \frac{1}{L} \int_0^T dt \langle \Psi(t)|\hat{J}_x|\Psi(t)\rangle, \tag{1.12}$$

it can be non-zero, and in this case it has to be an integer (provided adiabatic conditions, that is T long enough). Hence, the adiabatically pumped charge is quantized, and $Q \neq 0$ cases are originated by non-trivial topological features of the insulator.

In absence of external potential vector, the total current operator is $\hat{J} = \frac{\hat{p}}{m}$, with $\hat{p}$ the momentum and m the mass, so $\hat{J}$ can be identified with the velocity. Indeed

$$\begin{aligned} \langle\Psi|\frac{p}{m}|\Psi\rangle &= \frac{1}{2m}\left(\langle\Psi|p\Psi\rangle + \langle p\Psi|\Psi\rangle\right) = \\ &= \int_{-\infty}^{+\infty} \Psi^*(x)p\Psi(x) - (p\Psi(x))^*\Psi(x) = \\ &= \int_{-\infty}^{+\infty} j(x)dx \end{aligned} \tag{1.13}$$

where obviously $p = -i\partial_x$. To be more precise, one should specify the normalization, but the important aspect now is that $\hat{J} \propto \frac{\hat{p}}{m}$.

If one considers now a specific system, for example free electrons in 2D. Said x and y the propagation directions, one imposes periodic boundary conditions (PBC), with lenghts

L_x and L_y respectively. Also we set $\frac{L_x}{L_y} \ll 1$. The system is then essentially analogue to a cilinder, or to a torus closed as a ring. Thus, the following Schrodinger problem has to be solved:

$$\begin{aligned}
&(\frac{{p_x}^2}{2m} + \frac{{p_y}^2}{2m})\Psi(x,y) = E\Psi(x,y) \\
&\Psi(x+L_x,y) = \Psi(x,y) \\
&\Psi(x,y+L_y) = \Psi(x,y)
\end{aligned} \tag{1.14}$$

If one insert tubular flux ϕ along y direction, coaxial with the torus, then the Hamiltonian becomes

$$H(\phi) = \frac{(p_x + \frac{e\phi}{cL_x})^2}{2m} + \frac{{p_y}^2}{2m} \tag{1.15}$$

with same PBC as before.Associated Schrodinger problem can be solved using the unitary transformation

$$\tilde{H}_k = e^{ikx} H(\phi) e^{-ikx} \tag{1.16}$$

since $H(\phi)\Psi = E\Psi$ and $\tilde{H}_k\tilde{\Psi} = E\tilde{\Psi}$ have the same solution. We have to care tho about an important detail: while Ψ are periodical, from what discussed above it emerges $\Psi = e^{-ihx}\tilde{\Psi}$, so $\tilde{\Psi}$ are not periodical. New condition is then $\tilde{\Psi}(x+L_x,y) = e^{ihL_x}\Psi(x,y)$. Using the canonical transformation, $e^{ikx}p_x e^{-ikx} = p_x - \hbar k$ and so

$$\tilde{H}_k = \frac{(p + \frac{e\phi}{cL_x} - \hbar k)^2}{2m} + \frac{{p_y}^2}{2m} \tag{1.17}$$

Thus, choosing

$$\hbar k = \frac{e\phi}{cL_x} \rightarrow k = \frac{2\pi}{L_x}\frac{\phi}{\phi_0}, \tag{1.18}$$

$$\phi_0 = \frac{hc}{e}, \tag{1.19}$$

there is no more track of the flux ϕ in the Hamiltonian, even if still remains track in the PBC, that are now called twisted.
This is completely general and could be applied to the original Hamiltonian, Equation 1.10, which becomes

$$\hat{H}(k,t) = \sum_j \frac{(p_j + \hbar k)^2}{2m} + V_s(x_j) + V_l(x_j - vt)\frac{1}{2}\sum_{i\neq j} V_{int}(|x_i - x_j|) \tag{1.20}$$

and the current operator results

$$J = \frac{1}{\hbar}\frac{\partial \hat{H}(k,t)}{\partial k}\bigg|_{k=0} = \sum_j \frac{\hat{p}_j}{m} \tag{1.21}$$

All this argument is similar to the Bloch theorem: the system is in a static periodic potential and wavefunctions are of the kind $\Psi_{nk}(x) = e^{ikx}U_{nk}(x)$, where n is the band index and U_{nk} is periodic. Also, we are in first Brillouin zone (BZ), and the dispersion relation is $\hat{H}\Psi_{nk} = \varepsilon_{nk}\Psi_{nk}$. Equation satisfied by $U_{nk}(x)$ is

$$\hat{H}(k) = e^{-ikx}\hat{H}e^{ikx} - \frac{(p+\hbar k)^2}{2m} + v(x) \tag{1.22}$$

thus

$$\hat{H}(k)U_{nk}(x) = \varepsilon_{nk}U_{nk}. \tag{1.23}$$

Considering now a slow evolution and using the adiabatic theorem we get for the average current

$$\begin{aligned} &< \Psi(t)|\hat{J}|\Psi(t) >= \wedge < \phi_0(t)|\frac{1}{\hbar}\frac{\partial \hat{H}}{\partial k}|\phi_0(t) > \quad + \\ &+ i\sum_{n\neq 0}\left(\frac{< \phi_0(t)|\frac{\partial \hat{H}}{\partial k}|\phi_n(t) >< \phi_n(t)|\partial_t\phi_0(t)}{E_n - E_0} - c.c.\right) \end{aligned} \tag{1.24}$$

Performing some calculations, recalling the spectral representation of Berry phase, considering the fact that the considered system is an insulator, and that the BZ is periodized, and using the previous defined Bloch Hamiltonian, one can finally get

$$< \Psi(t)|\hat{J}|\Psi(t) >= -i\sum_{\nu}^{occ.}\sum_{k}^{BZ}\Big[< \partial_k U_{\nu,k}|\partial_t U_{\nu,k} - c.c]\Big] \tag{1.25}$$

So, finally, one can compute the charge passing during a period $[0,T]$ from one side of the sample to the other, dividing the current by the lenght L of the sample (taking then the limit $L \to \infty$ and integrating over time:

$$\begin{aligned} Q &= \lim_{L\to\infty}\frac{1}{L}\int_0^T dt < \Psi(t)|\hat{J}|\Psi(t) >= \\ &= -\sum_{\nu}^{occ.}\int_{-\frac{\pi}{a}}^{+\frac{\pi}{a}}\frac{dk}{2\pi}\int_0^T dti\Big[< \partial_k U_{\nu,k}|\partial_t U_{\nu,k} - c.c]\Big] = 0; \pm 1; \pm 2; ... \end{aligned} \tag{1.26}$$

where the quantization is due to the fact that the term between sqyare brackets is the Berry curvature, and the double periodicity in x and t guarantees the space has a torus topology. Hence, charge transported by an insulator could be non-zero.

1.3.2 Rice-Mele model

An explicit example of when this pumped charge is non-zero is the Rice-Mele (1982) model [Rice and Mele, 1982], whose Hamiltonian is

$$\hat{H}_{RM} = -J_1 \sum_{j=1}^{N} \left(\hat{c}^{\dagger}_{j,B} \hat{c}_{j,A} + H.c. \right) + \\ - J_2 \sum_{j=1}^{N} \left(\hat{c}^{\dagger}_{j+1,A} \hat{c}_{j,B} + H.c. \right) + \sum_{j=1}^{N} \left(\epsilon_A \hat{n}_{j,A} + \epsilon_B \hat{n}_{j,B} \right) \tag{1.27}$$

Here, A and B indicates the two sublattices, j is the index for the N cells, $\hat{c}^{\dagger}_{j,A/B}$ and $\hat{c}_{j,A,B}$ are the fermionic (creation and annihilation) operators and $J_{1/2}(t)$ and $\epsilon_{A/B}(t)$ are given by

$$J_1(t) = J_0 + \delta_0 cos \frac{2\pi t}{T} = J_0 + \delta(t) \tag{1.28}$$

$$J_2(t) = J_0 - \delta_0 cos \frac{2\pi t}{T} = J_0 - \delta(t) \tag{1.29}$$

$$\epsilon_A(t) = \epsilon_0 + \Delta_0 sin \frac{2\pi t}{T} = \epsilon_0 + \Delta(t) \tag{1.30}$$

$$\epsilon_B(t) = \epsilon_0 - \Delta_0 sin \frac{2\pi t}{T} = \epsilon_0 - \Delta(t) \tag{1.31}$$

Setting the zero of the energy such that $\epsilon_0 = 0$ and using the PBC, one could expand in Fourier series, defining the Bloch-Wannier transformations:

$$\hat{c}^{\dagger}_{k,A/B} = \frac{1}{\sqrt{N}} \sum_{j=1}^{N} e^{ikaj} \hat{c}^{\dagger}_{j,A/B} \hat{c}^{\dagger}_{j,A/B} = \frac{1}{\sqrt{N}} \sum_{k}^{N} e^{-ikaj} \hat{c}^{\dagger}_{k,A/B} \tag{1.32}$$

where N is the number of unit cells making up a big periodically-repeated lattice of length L = Na (i.e., wrapped-up on a circle). Consequently, the discrete wave-vectors allowed are

$$k = \frac{2\pi n}{Na} = \frac{2\pi n}{L} \quad with \quad n \in \mathbb{Z} \tag{1.33}$$

So, Hamiltonian becomes

$$\hat{H}_{RM}(t) = \sum_{k \in \mathrm{BZ}} \left[\hat{c}^{\dagger}_{k,A} \ \hat{c}^{\dagger}_{k,B} \right] \left[\hat{H}(k,t) \right] \begin{bmatrix} \hat{c}_{k,A} \\ \hat{c}_{k,B} \end{bmatrix} \tag{1.34}$$

where

$$\hat{H}(k,t) = \mathbf{R}(k,t) \cdot \hat{\sigma} = R_x(k,t)\hat{\sigma}_x + R_y(k,t)\hat{\sigma}_y + R_z(k,t)\hat{\sigma}_z \tag{1.35}$$

Simple calculations lead to

$$R_x(k,t) = -J_1(t) - J_2(t) \cos ka R_y(k,t) = -J_2(t) \sin ka R_z(k,t) = \Delta(t) \tag{1.36}$$

It is important to notice that $\mathbf{R}(k,t) = n\mathbf{R}(k,t+T), \quad \mathbf{R}(k,t) = \mathbf{R}(k+\frac{2\pi}{a},t)$. Thus, for every k, the effective magnetic field acting on the pseudo-spin-1/2 lattice is periodic both in k and in t, with periods $\frac{2\pi}{a}$ and T respectively. The projection of $\mathbf{R}$ on the x-y plane is a circumference of radius J_2, so three cases are possible:
1) $J_1 > J_2$: the circumference stays on the left of the origin without including it
2) $J_1 < J_2$: the circumference involves the origin
3) $J_1 = J_2$: the circumference touches the origin
The topological features of case 1) and 2) above are very different: in the first case the magnetic field does not wind around the origin, while in the second case it does so.
Eigenvalues of $\hat{H}$ are

$$\epsilon_{k,\pm}(t) = \pm|\mathbf{R}(k,t)| = \pm\sqrt{{J_1}^2 + {J_2}^2 + 2J_1J_2\cos ka + \Delta^2} \tag{1.37}$$

so, in Rice-Mele model working with PBC, there are two bands: a lower band $\epsilon_{k,-}(t)$ and an upper band $\epsilon_{k,+}(t)$, which are separated by a gap provided that $|\mathbf{R}| \neq 0$, that is guaranteed since $|\mathbf{R}| = 0$ means a gapless metallic situation where $J_1 = J_2 = J_0$ and $\Delta = 0$, which is never encountered during the dynamics. Indeed, one can imagine dynamics in the 2D plane, with $J_1 - J_2$ in the x-axis and Δ in the y-axis, as an ellipse wrapping around the critical gapless point $J_1 - J_2 = 0, \Delta = 0$.

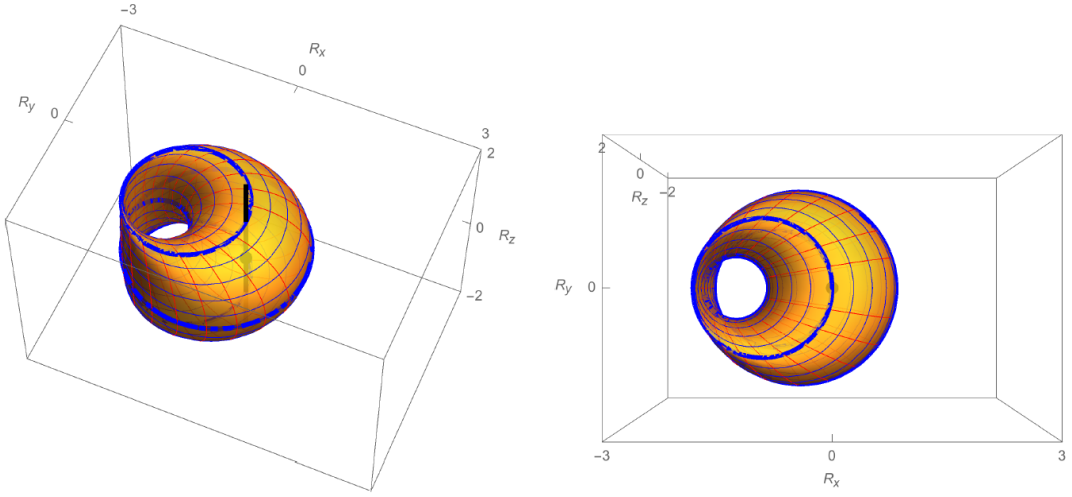

FIGURE 1.9: Parametric plot of $\mathbf{R}$(k, t) when k spans the BZ and t the period [0, T]. The surface has the topology of a torus: on the right, a top view of such torus.

If the number of electrons is half the number of lattice sites (that is the so called half filling), then the system is a band insulator, and the lower band of energy $\epsilon_{k,-}(t)$ is fully occupied. Working in tight-binding the associated $|U_{k,-}(t)>$ is a two-component spinor telling the amplitude for staying on the Wannier orbital centered on sublattice A or B in the unit cell. Hence, at half-filling the spinors $|U_{k,-}>$ constitute a completely filled

band, while $|U_{k,+}>$ is an empty band. Hence, the charge pumped in a period becomes:

$$Q = -\int_0^T dt \int_0^{\frac{2\pi}{a}} \frac{dk}{2\pi} i \left[< \partial_k U_{k,-} | \partial_t U_{k,-} > - < \partial_t U_{k,-} | \partial_k U_{k,-} > \right] \tag{1.38}$$

With a few calculations and changes of variables, one can recall the Berry curvature $\mathbf{B}$ and write

$$i \left[< \partial_k U_{k,-} | \partial_t U_{k,-} > - < \partial_t U_{k,-} | \partial_k U_{k,-} > \right] = \sum_{i<j} \mathbf{B}_{ij}(\mathbf{R}(k,t)) J_{ij}(k,t) \tag{1.39}$$

That is, in terms of the Berry curvature for a spin-1/2 problem:

$$\mathbf{B}_{ij} = i \left[< \partial_{R_i} U_-(\mathbf{R}) | \partial_{R_j} U_-(\mathbf{R}) > - < \partial_{R_j} U_-(\mathbf{R}) | \partial_{R_i} U_-(\mathbf{R}) > \right] = \epsilon^{ijk} \frac{R_k}{2|\mathbf{R}|^3} \tag{1.40}$$

Thus, the pumped charge for the Rice-Mele model is

$$Q = -\int_0^T dt \int_0^{\frac{2\pi}{a}} \frac{dk}{2\pi} \sum_{i<j} \mathbf{B}_{ij}(\mathbf{R}(k,t)) J_{ij}(k,t) = -c_1 \tag{1.41}$$

with c_1 the first Chern number, and it is the integral of the Berry curvature of the whole surface spanned by $\mathbf{R}(k,t)$, that explicitly is

$$c_1 = \int_0^T dt \int_0^{\frac{2\pi}{a}} \frac{dk}{2\pi} \frac{\mathbf{R}}{|\mathbf{R}|^3} \cdot \left(\frac{\partial \mathbf{R}}{\partial k} \times \frac{\partial \mathbf{R}}{\partial t} \right) \tag{1.42}$$

where

$$\left(\frac{\partial \mathbf{R}}{\partial k} \times \frac{\partial \mathbf{R}}{\partial t} \right) dt dk \tag{1.43}$$

is the element of area in the surface integral. Most crucial thing to notice is that this object is topological in nature, i.e. it must be an integer. Since the torus encloses the singularity at $\mathbf{R}^* = 0$, then the solid angle through which the Berry flux goes is 4π, but the monopole "charge" is $1/2$, and there is an extra factor $1/2\pi$ in the definition of c_1: thus, $c_1 = \pm 1$ is expected. The sign depends on how the surface $\mathbf{R}(k,t)$ is oriented, orientation that is decided by

$$\left(\frac{\partial \mathbf{R}}{\partial k} \times \frac{\partial \mathbf{R}}{\partial t} \right) \tag{1.44}$$

and points outward or inward depending on the direction in which the phase $\phi(t)$ is changed.

Chapter 2

Topologically protected magnetoelectric switching in $GdMn_2O_5$

2.1 Topologically protected magnetoelectric switching in a multiferroic

This is the title of the article published on 6th of July 2022 on Nature 607 [Ponet et al., 2022], which establishes a new paradigm for topologically protected phenomena in ferroic materials, specifically focusing on the magnetoelectric switching behaviour of $GdMn_2O_5$.

This phenomenon is crucial both for the understanding of the microscopic mechanisms of magnetoelectric coupling, and the role of topological protection, and for the field of permanent storage technology and data-processing devices. The ultimate goal of this devices is indeed the control of stable robust states in the storage medium, goal that can be pursued by controlling magnetism through electric fields, and vice versa, in order to significantly improve the energy efficiency.

The magnetoelectric switching behaviour observed depends on the magnetic field orientation, and shows three distinct switching regimes, sweeping the field up and down twice. The first and the third are two two-states switching regimes, which don't show any topologically protected properties, while the middle one, which is a four-states switching regime, shows a topologically protected behaviour.

This regime gives rise to a full 360° unidirectional rotation by half of the spins, in approximately 90° increments during the field swepts. This represent the microscopic analogue of a crankshaft, converting linear changes of the field into a rotational motion of the spins. Also, it acts like a binary counter, counting the number of field pulses modulo two, with high and low polarization represented by 0 and 1 respectively.

Furthermore, the four-states switching regime is topologically distinct from the other two two-states regimes, and, what's more, this middle regime is topologically protected by these two two-states switching regimes.
A non-zero integer winding number characterizes this peculiar state, acting as topological invariant.

2.2 Structure and properties of $GdMn_2O_5$

The multiferroic $GdMn_2O_5$ has a centrosymmetric crystal lattice with *Pbam* (#55 in International Tables) space-group simmetry.
Octahedrically coordinated Mn^{4+} ions and pyramidally coordinated Mn^{3+} ions form zigzag chains along the a axis with antiferromagnetic (AFM) exchange interactions between neighbouring spins along the chains. Interchain exchange interactions are relatively weak and geometrically frustrated, as Mn ions from neighbouring chaoìins form AFM pentagons.

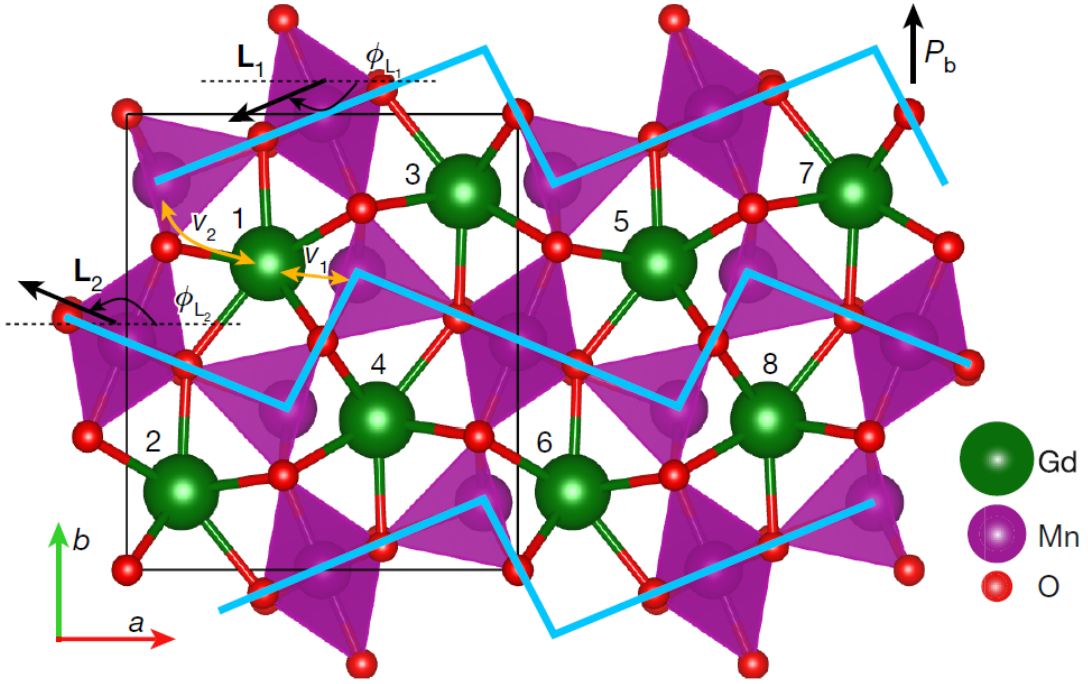

FIGURE 2.1: **Magnetic unit cell of $GdMn_2O_5$.** Mn ions (purple spheres) form zigzag chains (cyan lines) along the a axis with AFM intrachain interactions between Mn spins. $\mathbf{L}_1$ and $\mathbf{L}_2$ are the Néel vectors for the two distinct chains, forming angles ϕ_1 and ϕ_2 with the a-axis. Gd ions (green spheres) are inside pentagons formed by Mn ions from the neighbouring chains. Red spheres are O ions, mediating superexchange interactions. The boundary of the structural unit cell is marked by the black box. The yellow arrows denote the exchange paths between Gd and the chains, which correspond to ν_1 and ν_2 in the model.

$GdMn_2O_5$ orders magnetically at at the Néel temperature $T_{N1} = 40$ K, adopting an incommensurate state with the propagation vector q = (0.49, 0, 0.18). Below the commensurate–incommensurate transition temperature $T_{N2} = 33$ K, it locks into a commensurate state with q = (1/2, 0, 0), showing one of the highest magnetically induced electric polarizations of 3600 μCm^{-2}, and a large variation (up to $5,000$ μCm^{-2}) in an applied magnetic field. This field-induced polarization variation is robust and changes very little when multiple field sweeps are applied. The electric polarization is induced by Heisenberg exchange striction on both Mn–Mn and Mn–Gd bonds, and has a large electronic component.

2.3 Primordial experimental results

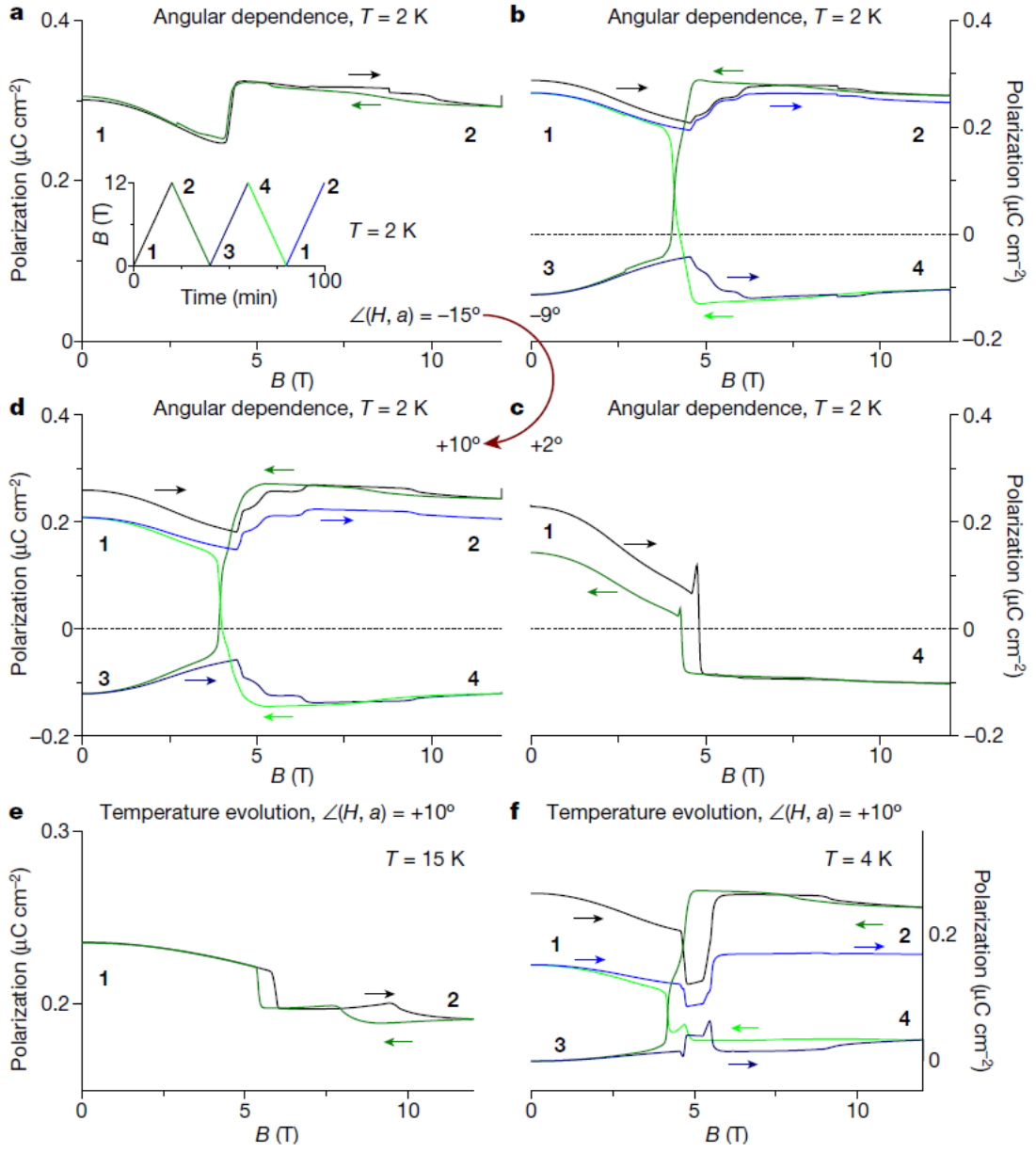

FIGURE 2.2: **Evolution of the electric polarization loop across critical angle and critical temperature**. **a-d**, Field dependence of the electric polarization of $GdMn_2O_5$ for different off-axis orientations of the applied magnetic field. **a,c**, Conventional two-state switching is observed if magnetic field angle is far larger than the 'magic' direction (a) or very close to the crystallographic a axis (c). **b,d**, Unusual four-state hysteresis loop for the magnetic-field direction close to the magic angle of ±10°. Similar behaviour can be observed in plots (b) and (d), demonstrating the symmetry between positive and negative external field angles. The inset shows the sequence of the magnetic field sweeps. The labels 1–4 mark the four polarization states. The arrows show the direction of magnetic-field-change during the sweep. The experiments were carried out at T = 2 K. **e**, At high temperatures, only a small step is seen at the transition that shows some hysteresis and the two-state switching. **f**, Four-state switching starts to appear approximately below T = 5 K.

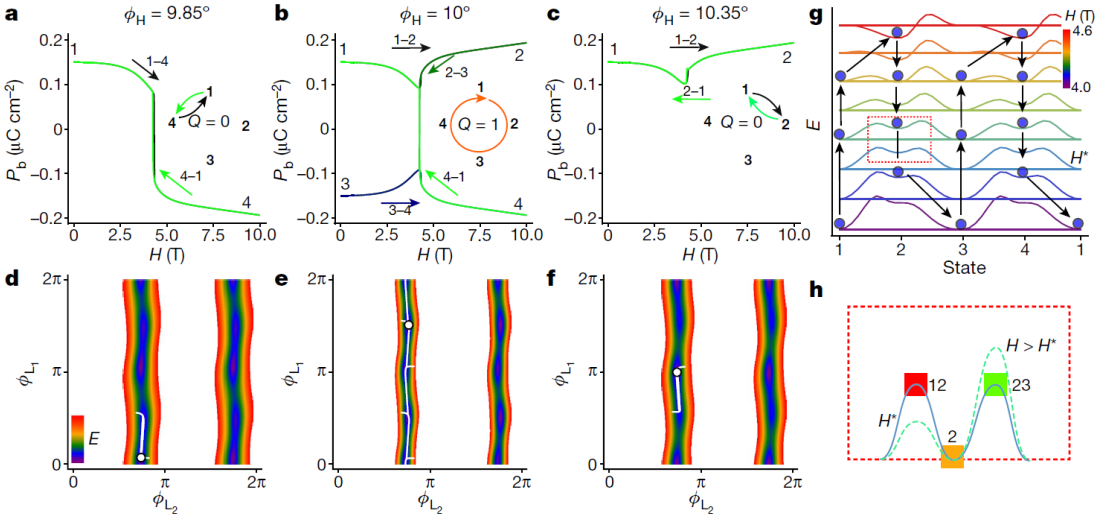

FIGURE 2.3: **Simulation of magnetoelectric switching**. **a-c**, Evolution of electric polarization P_b during the magnetic field sweep cycle for various magnetic field orientations. In each panel, the changes of the curve colour indicate the same progression of the sweep cycle as in Fig. 2.2. The four-state switching is seen for the field at the magic orientation. The insets indicate the corresponding switching paths and winding numbers. **d–f**, Trajectories (in white) in the space of the Néel vectors' orientations (ϕ_{L_1}, ϕ_{L_2}), through the field sweep cycles in different regimes. The colour map shows the energy landscape in the vicinity of the switching fields, with higher energy encoded by the red colour. The dots represent the position of the system along the trajectory at which the energy landscape is depicted. **g**, Evolution of transition barriers between states 1, 2, 3 and 4 as the magnetic field at 10° to the a-axis is swept through the hysteresis region. The plots are shifted vertically, and colour-coded to distinguish the magnetic field strengths. Here the parameters were slightly altered to increase the width of the hysteresis region for illustrative purposes. The arrows and blue dots denote the trajectory of the energy minimum during the field sweep. Coordinated changes of the state energies and barrier asymmetry with magnetic field enable the topological behaviour. **h**, Schematic evolution of the barriers connecting state 2 to states 1 and 3 in the vicinity of H*. Saddle-point states are denoted by 12 and 23.

The great difference between this study and the previous ones, is that in this work are performed multiple experiments with field titlted away from a axis, in the a-b plane at different ϕ_H (while in the previous studies the field was only applied parallel to the a axis).

Figure 2.2 shows the evolution of the electric polarization in $GdMn_2O_5$ as a function of this external magnetic field.

The ferroelectric polarization hysteresis curves are heavily effected by this tilting.

For temperatures above about 5K, around the magnetic field $H = 6$ T, a field-induced reorientation is observed, which gives place to a small hysteresis loop (in agreement with previous results for $H||a$). Below 5 K, and for field intensities around 5 T, an unusual hysteresis loop opens, as it can be seen in [insert picture]. The main feature of this loop is, at low temperatures, its remarkable deterministic four-state cycle with polarization reversals, repeatable by applying further sweeps. The electric polarization is not changed

much by the transition from state 1 to state 2 or from state 3 ti state 4 upon increasing the magnetic field intensity. Nonetheless, it is the decrease of the magnetic field that transforms state 2 into state 3, and state 4 into state 1, resulting in the reversal of the electric polarization.
A precise region for the direction of the magnetic field in order to get this loop has been found by doing further systematic experiments with tilted magnetic fields. The four-states sequence has not been observed if the magnetic field is either close to the a axis within $\pm 6^\circ$ or if it is outside the $[-11^\circ, +11^\circ]$ interval, where only two of the four branches are cycled through. As we can see in [insert picture], they are $1 \rightarrow 2$ or $1 \rightarrow 4$. This distinctive magnetoelectric switching is then observed around two magic angles: $\pm\phi_H^*$, where $\phi_H^* \approx 10^\circ$.
It is also remarkable to notice that the magic angle roughly matches the orientation of Mn and Gd spins in zero field in one of the AFM chain.

2.4 Modelling

The first model created and described in this work to explain this peculiar switching behaviour, is built using a model of two interacting Mn chains [refer to picture] and eight Gd spins per unit cell, coupled to external magnetic and electric fields. Since AFM interchain exchange interactions are dominant in RGd_2O_5 systems, neighbouring Mn spins are assumed to remain largely antiparallel within each chain, at all applied magnetic fields, thus they can be described by two Néel vectors. Hence, the state can be described using two main set of parameters:
$\mathbf{S}_i$, where i = 1,...,8, for Gd spins, and unit vectors $\mathbf{L}_\alpha$, where $\alpha = 1, 2$, for the AFM order parameters of the two inequivalent chains, inside the magnetic unit cell. Note: $\mathbf{L}_\alpha$ make angles ϕ_{L_α} with a axis (as shown in Figure 2.1). In order to build the Hamiltonian density, it has to be considered also that Heisenberg exchange striction induces an electric polarization P_b (as the result from the interaction between the spins and the magnetic field), which contributes proportionally to $\mathbf{L}_1 \cdot \mathbf{L}_2$, and a similar one originating from the Gd-Mn bonds. Neglecting quantum effects for large Gdf spins (nominally $S = 7/2$),

the Hamiltonian density (enrgy per magnetic unitc cell) thus results

$$\begin{aligned}
H = {} & \gamma(\mathbf{L}_1 \cdot \mathbf{L}_2)^2 + \sum_a \chi \left((\mathbf{H} \cdot \mathbf{L}_a)^2 - H^2 \right) + \\
& - K_L \sum_a (\mathbf{L}_a \cdot \mathbf{n}_a{}^2 - \sum_i (K_S (\mathbf{N}_i \cdot \mathbf{S}_i)^2 + g\mu_B \mathbf{H} \cdot \mathbf{S}_i) + \\
& + \frac{1}{2}(g\mu_B)^2 \sum_{i \neq j} \left(\frac{\mathbf{S}_i \cdot \mathbf{S}_j}{r_{ij}^3} - 3 \frac{(\mathbf{S}_i \cdot \mathbf{r}_{ij})(\mathbf{S}_j \cdot \mathbf{r}_{ij})}{r_{ij}^5} \right) + \\
& + \sum_{i,\alpha} V_{i\alpha} \mathbf{S}_i \cdot \mathbf{L}_\alpha + \\
& - P_b [8\beta_1 (\mathbf{L}_1 \cdot \mathbf{L}_2) + (\mathbf{S}_1 - \mathbf{S}_5)(\beta_2 \mathbf{L}_2 + \beta_3 \mathbf{L}_1) + \\
& + (\mathbf{S}_2 - \mathbf{S}_6)(\beta_2 \mathbf{L}_1 + \beta_3 \mathbf{L}_2) + \\
& + (\mathbf{S}_3 - \mathbf{S}_7)(\beta_2 \mathbf{L}_2 + \beta_3 \mathbf{L}_1) + \\
& + (\mathbf{S}_4 - \mathbf{S}_8)(\beta_2 \mathbf{L}_1 + \beta_3 \mathbf{L}_2)] + P_b^2/2
\end{aligned} \tag{2.1}$$

In this expression are introduced several parameters: the easy-axis anisotropies K_L and K_S, respectively referred to the AFM order $\mathbf{L}$ and spins $\mathbf{S}$; $\mathbf{n}_\alpha$ and $\mathbf{N}$'i are unit vectors along the easy-axes; g is the Landé factor; μ_B is the Bohr magneton; γ is $\gamma \approx \frac{J_\perp^2}{J_\parallel} > 0$, where $J_\perp$ is the interchain exchange and $J_\parallel$ is the interchain AFM exchange. The first term of the Hamiltonian represents indeed the competition between interchain exchange and interchain AFM exchange: it describes the lowering of the energy due to spin canting, possible when $\mathbf{L}_1$ and $\mathbf{L}_2$ are non-collinear.

The first term originates from the competition of the interchain exchange $J_\perp$ and the intrachain AFM exchange $J_\parallel$, with $\gamma \approx \frac{J_\perp^2}{J_\parallel} > 0$. It describes the energy lowering owing to spin canting, possible when $\mathbf{L}_1$ and $\mathbf{L}_2$ are non-collinear. The second term represents the Zeeman energy of the antiferromagnetically ordered Mn spins canted by the field, with χ being the susceptibility perpendicular to $\mathbf{L}$; K_L and K_S are easy-axis anisotropy constants of Mn and Gd spins. Subscripts L and S refer to AFM order $\mathbf{L}$ and spins $\mathbf{S}$; $\mathbf{n}_\alpha$ and $\mathbf{N}_i$ are unit vectors along the easy axes, respectively, and g and μ_B are the Lande factor and the Bohr magneton. The third line describes the dipole–dipole interactions between Gd spins, which were restricted to five nearest neighbours. The Heisenberg exchange constants $V_{i\alpha}$ describe Mn–Gd interactions, where $V_{i\alpha} = v_1$ for the exchange constant between the Gd and the Mn chain, containing the nearest (pentahedrally co-ordinated) Mn ion, and v_2—the exchange coupling to the other Mn chain. The terms with $\beta_{1,2,3}$ describe the magnetoelectric interactions between P_b and $\mathbf{L}_\alpha$ and $\mathbf{S}_i$, the last term being the dielectric energy.

It's been verified that including further neighbours up to 8.5 $\overset{\circ}{A}$ within the a–b plane or neighbours along the c direction at 6.5 $\overset{\circ}{A}$ does not change the results qualitatively.

It is important to notice that this model is phenomenological and not microscopic: this implies a non-direct relation between model parameters and microscopic interactions. Indeed, in it are involved $\mathbf{L}_\alpha$ and $\mathbf{S}_i$ instead of all microscopic degrees of freedom. This was mandatory to minimize model complexity. It is because of this that determining the exact values of the parameters from ab initio simulations is a very hard task.
Going back to discussing how this model describes the system, it should be mentioned that the commensurate multiferroic state at zero field is four-fold degenerate as it breaks both time-reversal symmetry and inversion symmetry:

$$\begin{aligned} T &: (\mathbf{L}_1, \mathbf{L}_2) \rightarrow (-\mathbf{L}_1, -\mathbf{L}_2) \\ I &: (\mathbf{L}_1, \mathbf{L}_2) \rightarrow (-\mathbf{L}_1, \mathbf{L}_2) \end{aligned} \tag{2.2}$$

This implies that states related by time-reversal symmetry have the same electric polarization, while states related by inversion symmetry have opposite signs polarizations. Here it comes one of the crucial steps both for this work's simulations and for the further ones we have performed: the tracking of the (local) energy minimum through the energy landscape. This tool is the key for understanding how the barriers of the potential energy surface transform giving place to the different states. The starting point of these simulations in one of the system's four degenerate ground states with zero magnetic field. Then, the minimum is tracked while ramping magnetic field's strength up and down, as field induced transitions occur at spinodal points, at which system's metastable state becomes unstable.
Tuning the parameters to describe experimental results, especially to reproduce the experimental hysteresis loop for the four-state switching, as close as possible, resulted in the simulations shown in Figure 2.3. It emerges a relatively narrow magic-angle region (even though exact position of the minimum and extension of the region can be tuned by varying model parameters). This region is itself remarkably robust. Therefore, this model reproduces the experimentally observed four-state switching regime at the magic angle $\phi_H^* = 10^\circ$ and the switching between states 1 and 2 with close values for electric polarization for $\phi_H > \phi_H^*$. It is natural at this point to deepen the discussion about this four-state switching at the magic angle. Mn and Gd spin configuration are displayed in Figure 2.4, in the right green box.

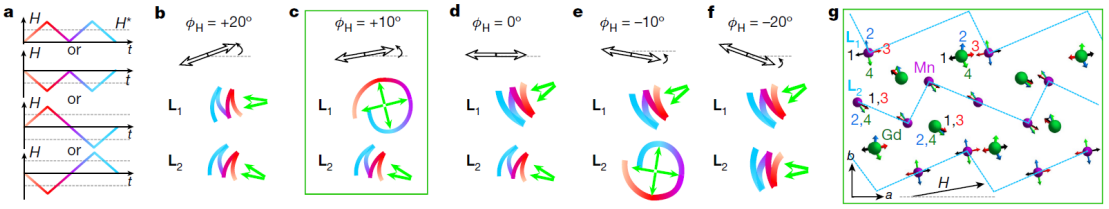

FIGURE 2.4: Magnetoelectric switching regimes. **a** Time dependence of the magnetic field. The field is tilted by the angle ϕ_H away from the a-axis. Colour coding is used to indicate the synchronous evolution of the Néel order parameters, $\mathbf{L}_1$ and $\mathbf{L}_2$ in**b-f**. For a fixed ϕ_H, each of the shown magnetic-field ramp protocols (positive or negative field ramps) leads to the same result. **b** Two-state switching for large positive ϕ: $\mathbf{L}_1$ and $\mathbf{L}_2$ toggle between two orientations. **c** Four-state switching in the positive magic-angle interval: $\mathbf{L}_1$ rotates, whereas $\mathbf{L}_2$ toggles, as shown in **g**. **d** Two-state switching at small ϕ_H: both order parameters toggle between two orientations. **e** Four-state switching at the negative magic angle: $\mathbf{L}_1$ toggles, whereas $\mathbf{L}_2$ rotates in the direction opposite to that of $\mathbf{L}_1$ in **c**. **f** Two-state switching for a large negative ϕ_H: both order parameters toggle between two orientations. **g** Spin configurations 1–4 in the magnetic unit cell, visited in the switching process at $\phi_H = 10°$.

In the low-field states 1 and 3, Mn spins align close to the anisotropy axes of the two chains, with the Gd spins aligning generally antiparallel to the closest Mn spin, to which they are strongly coupled (ν_1 in Figure 2.1). This causes a roughly left–left–right-right sequence of the Gd spins. In the high-field states 2 and 4, Mn spins orient nearly orthogonal to the magnetic field owing to the Zeeman interactions. The Gd spins are again influenced mostly by the AFM exchange with the nearest Mn ion, while being tilted slightly towards the external magnetic field. These simulations have hence found in this tilting one of the most contributing factors to the peculiar unidirectional switching behaviour, since it guides the rotation of Mn spins. In Figure 2.3 d-f is illustrated the typical energy landscape in the (ϕ_{L_1}, ϕ_{L_2}) space, calculated for three different values of ϕ_H and at field magnitudes that highlight the differences between the three regimes. This landscape is here consisting of two narrow valleys elongated in the ϕ_{L_1} direction and separated by the angle π in the ϕ_{L_2} direction. This means that through the field sweeps half of the states are accessed (among the four low-field states and the four high-field states).

Zeeman and anysotropy energies of Mn spins in chain 1 compete resulting in an approximate energy independence of the direction of $\mathbf{L}_1$ near the switching field. Because of this, the magnetic field is tending towards an easy-axis (as indicated by the black arrow in the right green box of Fig. 2.4), possibly allowing for a degree of electric control of the magnetic configuration, owing to the coupling between the polarization and the soft magnetic mode. This consideration about the possibility of an electric control of magnetism is one of the leitmotiv for this thesis work, so it will be crucial in our further discussions and here are the grounds. A similar flattening of the energy surface occurs in textbook antiferromagnets near the spin-flop transition, where at a critical field applied

along the easy axis, the spins flip perpendicular to the field to lower the Zeeman energy by canting towards it. The important difference of the behaviour discussed here is that the direction in which the spins progress during the up-and-down sweeps is unambiguous: the spins rotate unidirectionally throughout the cycling.

Another way to study the evolution of the system is in different regimes is to compare the trajectories (white lines in Fig. 2.3 d-f). It can be noticed that for all regimes, the field-dipendent state of the system is confined to a valley with ϕ_{L_1} varying much more than ϕ_{L_2}. In the topologically trivial regimes (Fig. 2.3d-f), the system remains in the neighbourhood of the starting point, with the trajectory contractible to a single point. In the four-state regime in Fig. 2.3e, the system progresses through the entire valley unidirectionally, connecting the top and bottom edges, with $\mathbf{L}_1$ rotating a full 360°. This path cannot be contracted to a single point, which highlights its topologically distinct nature compared with the other two regimes. The space we're considering is a two dimensional (ϕ_{L_1}, ϕ_{L_2}) space with a torus topology: for a trajectory in it, it can be possible to define a winding number

$$Q = \frac{1}{2\pi} \int_0^{t_0} dt (L_1^x \partial_t L_1^y - L_1^y \partial_t L_1^x) \tag{2.3}$$

Thus, it is immediate to compute Q for the two different types of regime. Integrating over the time interval t_0, during which the magnetic field is ramped up and down twice (so till the system goes back to the original state), is obtained Q= 0 for the two-state switching regime, while Q= 1 for the four-state switching regime. Here it emerges analytically the nature of the topological protection: as long as the two extremal two-state switching regimes are present, there will always exist a boundary region near the magic angle, interpolating between the two and leading to the circular four-state hysteresis, hence the four-state switching regime.

This is crucial because it gives rise to ground-breaking possibilities: since manipulating the values of the model parameters one can choose the exact position position and width of this topologically non-trivial region, it is reasonable to guess the existence of other materials that enable this peculiar behaviour, especially regarding multiferroic materials. It's been discovered that this is valid for a surprisingly wide range of parameters, which produces high hopes for further research in this field.

Through the model it has also been possible to understand the crankshaft behaviour of the system. Focusing on the orientation of Gd spins, it's been observed that, since they largely follow the chain they are most strongly coupled with, half of them undergo a full circle rotation, while the remaining half toggle back and forth together with $\mathbf{L}_2$. Therefore, in the topological regime, the material mimics the behaviour of a crankshaft: it transforms the back-and-forth changes of the external magnetic field (which has the role of the "piston") into a circular motions of the spins (which act like the "driveshaft").

Elastic string calculations have been performed to understand the unidirectional trajectory shown in Fig. 3e, when the field is oriented at magic angle $\phi_H^* \approx 10°$. These calculations aimed to investigate one of the key-point in the studying of this effect, that is the evolution of the barriers of the potential evolution surface, which separate the different states, shown in Figure 2.3 g. This is one of the main tool used also in this thesis work. The simulation started in the low-field state 1, which becomes metastable as the magnetic field increases. State 1 and 3 (and also 2 and 4) are related by spatial inversion that changes the sign of $\mathbf{L}_1$ and have equal energies $E_1 = E_3(E_2 = E_4)$, for any applied magnetic field, in apparent contradiction with the unidirectional evolution $1 \rightarrow 2 \rightarrow 2 \rightarrow 3 \rightarrow 4$. The resolution of this paradox lies in the fact that the energy barriers separating state 1 from states 2 and 4 are, in general, different, as the saddle-point states, 12 and 14 (Fig. 2.3 h), that determine the height of these barriers are not related by any symmetry transformation. Moreover, the evolution of these barriers in terms of the applied field is also asymmetric.

The asymmetry of these barriers has indeed also a key-role in this topological switching behaviour, and will be further investigated during this work.

The evolution of the barriers can be seen in Fig. 2.3 g. Top curve is calculated at field H_1, where state 1 becomes unstable and the barrier along $1 \rightarrow 2$ path disappears, while the barrier separating states 1 and 4 is still present. At lower field, at $H = H_2$ (on the downwards field ramp), state 2 becomes unstable and barrier between states 2 and 3 vanishes whereas states 2 and 1 are still separated by a barrier (bottom curve), leading to $2 \rightarrow 3$ transition. Increasing and decreasing the magnetic field again, the transition sequence $3 \rightarrow 4 \rightarrow 1$ occurs in precisely the same way, since the barrier states 34 and 12 (as 14 and 23) are related by inversion transformation (so $E_{34} = E_{12}$). The only difference is now the opposite sign of the polarization.

This evolution of the potential energy surface (PES) is equivalent to the previously described Thouless charge pump, particularly to the one induced by circular motion in the two-dimensional space of the Rice-Mele model (also discussed in previous chapters).

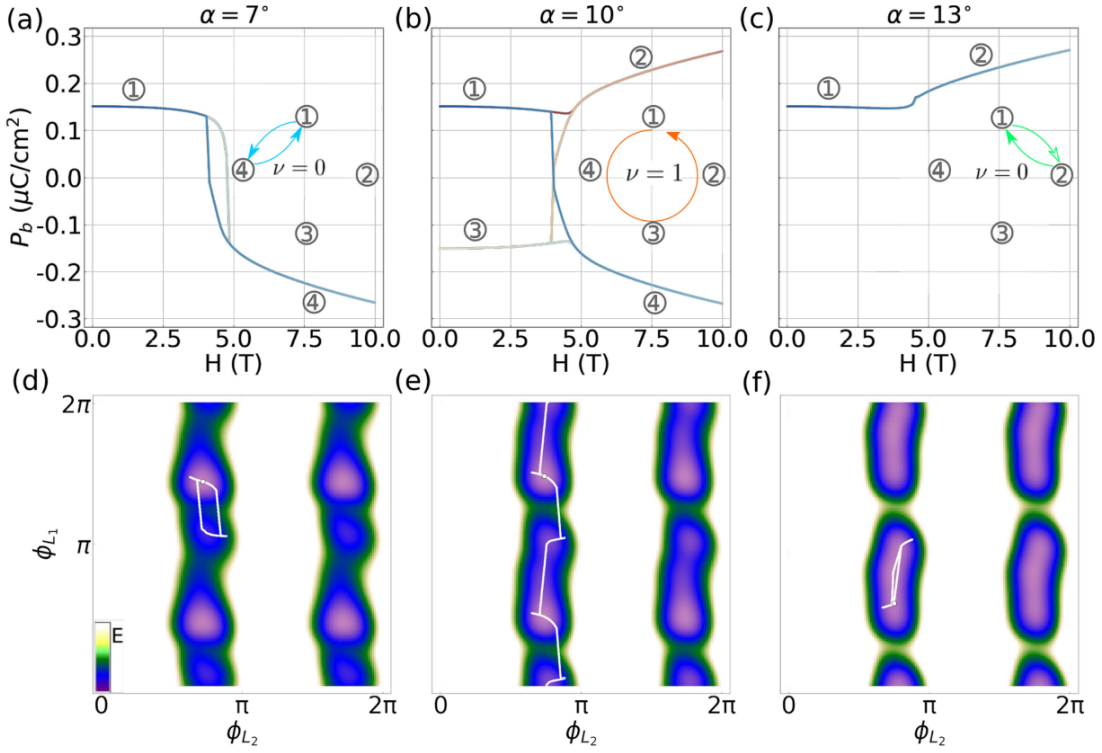

FIGURE 2.5: **a**–**c**: Evolution of electric polarization Pb during the magnetic field sweep cycle for various magnetic field orientations. In each panel, the changes of the curve colour from red to blue indicate the progression of the sweep cycle. The four-state switching is seen for the field at the magic orientation.The insets indicate the corresponding switching paths and winding numbers. **d**–**f**: Trajectories (in white) of AFM order parameter orientations (ϕ_{L_1}, ϕ_{L_2}) through the field sweep cycles in different regimes. The colour map shows the energy landscape at an intermediate H field.

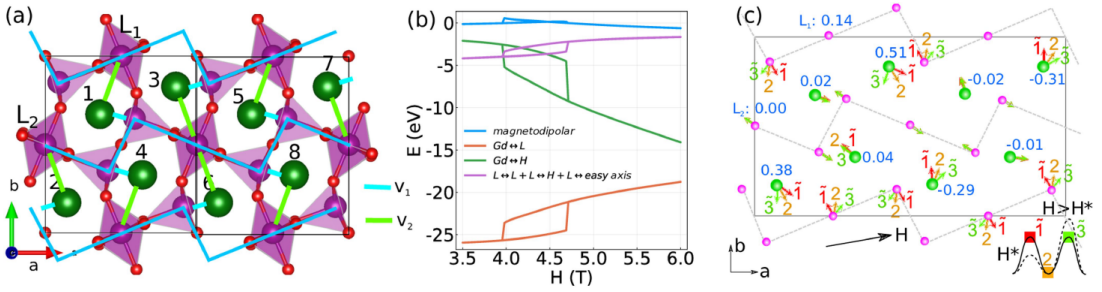

FIGURE 2.6: **a** Exchange interactions between Gd ions and neighbouring AFM Mn chains ($\nu_{1,2}$). Easy axes for $L_{1,2}$ coincide with the longer zigzag segments; for Gd – with blue lines indicating ν_1 exchange. **b** Field dependence of energy contributions: magnetodipolar interactions, Gd–Mn exchange, Zeeman energy of Gd spins and energy of antiferromagnetically ordered Mn spins, for the field pointing at 10° to the a axis. **c** Spin configuration in state 2 and in the states, corresponding to the saddle points at the barriers toward the neighbouring minima at H=H* (states and colour coding for spins is indicated in the inset). The numbers in blue show the field projections of magnetization difference of Gd and Mn ions in the saddle-point states. The difference of magnetization components along the field in two saddle-point states results in the asymmetric barrier evolution when the field is varied.

Chapter 3

Minimal Landau theory model

Topological switching behaviour observed in $GdMn_2O_5$ results from coordinated changes in the energies of the four states and the barrier asymmetries [Ponet et al., 2022]. The model described in Chapter 2 is complex and not easy to use in the effort of finding other materials that support this behaviour. Then, the necessity of a simpler model arises naturally from the promising prospect of further research. In order to do that, it is tempting to try to build a Landau-type model, deriving the transformation properties of the magnetic field and of the AFM order parameters X_1, X_2 from a symmetry analysis, taking advantage of the $GdMn_2O_5$ space group properties.
To be able to do this, it is useful to recall the different types of AFM and then it is necessary to discuss $GdMn_2O_5$ structure symmetries.

3.1 Magnetic ordering and symmetry breaking

Magnetic ordering is a symmetry-breaking process. Its understanding is deeply connected with symmetry reduction. The symmetry of a magnetic phase is given by the magnetic space group (MSG, or Shubnikov group) for a commensurate ordering, and by the magnetic superspace group (MSSG) for an incommensurate ordering [Perez-Mato et al., 2015]. The symmetry group of a magnetic phase determines all structural and magnetic symmetry constraints that are thermodynamically obliged within its whole stability range. These symmetry-dictated properties can only be broken through an additional phase transition or by applying a symmetry-breaking perturbation. Expressing the symmetry characterization of magnetic phases in the form of a symmetry group can lead to the prediction and understanding of their magneto-structural properties, and, similarly to what happens in crystallography, the assignment of some symmetry to a magnetic structure implies very specific constraints on the possible magnetic moments

and atomic positions, that is, they can be unambiguously defined and distinguished from other features that are not symmetry protected. Such study has been made easier thanks to the quite recent development of databases and software like the Bilbao Crystallographic Server Aroyo, Kirov, et al., 2006; Aroyo, Perez-Mato, et al., 2006 and Isotropy Suite software Campbell et al., 2006; Stokes et al., 2021 (that we used extensively in our analysis), which give an unambiguous and unified description of magnetic structures and enable a systematic application of magnetic symmetry information. In the following paragraphs, operations and symmetry that define the structure of $GdMn_2O_5$ will be obtained thanks to these tools.

3.2 Commensurate magnetic structures and the MSG

The case of our interest is the one of a commensurate ordering, so, as in the context of magnetic structure atomic magnetic moments can be considered real quantities, the action of time reversal operation simply changes the sign of all magnetic moments in the structure, while keeping the non-magnetic degrees of freedom unchanged. By definition, a commensurately ordered magnetic phase breaks the time reversal symmetry operation that is present in the magnetically disordered paramagnetic phase.

Said G the space group of the paramagnetic phase, considering the presence of the disordered atomic spins, we can describe the full symmetry using the grey magnetic group $G1'$, which can be decomposed in cosets as $G1' = G + \{1'|0,0,0\}G$. Grey groups are type II MSG (out of the four possible MSG), and they are the space groups with an additional anti-symmetry version of every symmetry operation, i.e. in addition to the operation of G, they include the time reversal operation. Then, the symmetry of a commensurately ordered magnetic phase is described by a subgroup of the parent group $G1'$, namely Ω, which does not include $\{1'|0,0,0\}$, meaning that Ω may include non-identity operations either combined or not combined with time reversal, but not both. Being commensurate, the lattice or a sublattice of the paramagnetic phase will also be maintained, and in general, Ω can be decomposed in cosets with respect to a subgroup F of G with the same lattice periodicity as Ω in one of the following three forms: $\Omega = F, \Omega = F + \{\mathbf{R}'_o|t\}F$, or $\Omega = F + \{1'|\mathbf{L}\}F$, where $\{\mathbf{R}'_o|t\}$ and $\{1'|\mathbf{L}\}$ are operations of the gray group $G1'$, and $\mathbf{L}$ is a specific lattice translation of the paramagnetic phase. For consistency, $\{\mathbf{R}'_o|t\}^2$ and $\{1'|2\mathbf{L}\}$ must belong to F, whereas $\{\mathbf{R}'_o|t\}$ and $\{1'|\mathbf{L}\}$ belong to G but not to F. These three types of possible magnetic symmetry breakings correspond to the three types of MSGs known as type I, III, and IV, respectively. All the symmetry operations present in MSGs of type I coincide with those of the ordinary space groups, but, as magnetic groups, the existence within the symmetry of the system of the same

operations combined with time reversal is explicitly discarded. The constraints coming from the MSG of a magnetic phase are robust (symmetry-protected) properties within the whole phase. Both atomic magnetic moments and atomic positions are subjected to it. Any operation $\{\mathbf{R'}|t\}$, which includes time reversal, acts on the atomic positions in the same way as the operation $\{\mathbf{R}|t\}$ without time reversal; therefore, the effective symmetry that constrains the atomic positions can be described by an effective space group H, which is either F, $F+\{\mathbf{R}|t\}F$, or $F+\{1|\mathbf{L}\}F$, depending on Ω being type I, III, or IV, respectively. In addition, the symmetry relations forced by the magnetic group on the atomic magnetic moments can be reduced to the following rule: If two atoms with nonzero magnetic moments have their atomic positions related by an operation of Ω, then their moments are related by the corresponding point-group operation $\mathbf{R}$ (transforming as axial vectors) with an additional change of sign if time reversal is included in the operation. For magnetic atoms at special positions, i.e. kept invariant by some of the operations of Ω, site-symmetry restrictions on the possible magnetic moments exist, and they are part of the definition of the Wyckoff positions of an MSG.

A full description of the symmetry properties of a magnetic phase requires the knowledge of both symmetries: $G1'$ (grey space group for the paramagnetic phase) and its subgroup Ω. More concretely, if H is the effective space group of the nonmagnetic degrees of freedom, described above, and s is its index with respect to G (i.e., the factor relating the number of operations in G and H), then $2s$ is the index of Ω with respect to $G1'$, and one can choose s operations g_j of G (coset representatives) not belonging to H, such that $G = H + g_2H + \cdots + g_sH$, and s equivalent, distinct, domain-related structures can be obtained by applying each operation g_j to the magnetic structure. An additional set of s trivially related domains, with reversed moments, corresponds to the application of the symmetry operations g'_j. The magnetic symmetry of a domain-related structure obtained by the action of g_j is given by the subgroup $g_j\Omega g_j^{-1}$ of $G1'$. This subgroup can coincide with Ω or be a distinct subgroup belonging to the same conjugacy class. Conjugate subgroups describe physically equivalent symmetry breakings.

3.3 $GdMn_2O_5$ space group and transformation properties

Taking advantage of the just explained tools, it is possible to provide an unambiguous and full description of the magnetic structure of the crystal by listing the atomic positions and magnetic moments of a set of symmetry-independent atoms within the unit cell, the so-called asymmetric unit.

The subject of our focus is $GdMn_2O_5$, whose parent space group is $Pbam$ (#55 in International Tables, Nespolo, 2017), while the magnetic space group is P_aca2_1 (#29.104),

which means that its symmetric and magnetic properties (that is its whole magnetic structure) are described by the following tables:

N	$(x, y, z)^b$	$(m_x, m_y, m_z)^c$	Seitz notation
1	$x, y, z, +1$	m_x, m_y, m_z	$\{1 \mid 0, 0, 0\}$
2	$-x+3/4, y+1/2, -z, +1$	$-m_x, m_y, -m_z$	$\{2_{010} \mid 3/4, 1/2, 0\}$
3	$-x+1/4, y+1/2, z, +1$	$m_x, -m_y, -m_z$	$\{m_{100} \mid 1/4, 1/2, 0\}$
4	$x+1/2, y, -z, +1$	$-m_x, -m_y, m_z$	$\{m_{001} \mid 1/2, 0, 0\}$
5	$x+1/2, y, z, -1$	$-m_x, -m_y, -m_z$	$\{1' \mid 1/2, 0, 0\}$
6	$-x+1/4, y+1/2, -z, -1$	$m_x, -m_y, m_z$	$\{2'_{010} \mid 1/4, 1/2, 0\}$
7	$-x+3/4, y+1/2, z, -1$	$-m_x, m_y, m_z$	$\{m'_{100} \mid 3/4, 1/2, 0\}$
8	$x, y, -z, -1$	$m_x, m_y, -m_z$	$\{m'_{001} \mid 0, 0, 0\}$

TABLE 3.1: Operations that define the MSG of the magnetic structure of $GdMn_2O_5$

Label	Atom type	x^a	y^a	z^a	Symmetry constraints on M	$M_x{}^b$	$M_y{}^b$	$M_z{}^b$	$\lvert M \rvert$
Gd1_1	Gd	0.06975	0.17160	0.00000	$m_x, m_y, 0$	4.87	1.63	0.0	5.14
Gd1_2	Gd	0.93025	0.82840	0.00000	$m_x, m_y, 0$	−4.51	−1.5	0.0	4.75
Mn1	Mn	0.00000	0.50000	0.25510	m_x, m_y, m_z	−2.85	0.95	0.0	3.00
Mn2_1	Mn	0.20590	0.35180	0.50000	$m_x, m_y, 0$	3.8	−1.27	0.0	4.01
Mn2_2	Mn	0.79410	0.64820	0.50000	$m_x, m_y, 0$	3.8	−1.27	0.0	4.01
O1	O	0.00000	0.00000	0.26970					
O2_1	O	0.07630	0.44860	0.00000					
O2_2	O	0.92370	0.55140	0.00000					
O3_1	O	0.07270	0.43560	0.50000					
O3_2	O	0.92730	0.56440	0.50000					
O4_1	O	0.19970	0.20760	0.24500					
O4_2	O	0.80030	0.79240	0.24500					

TABLE 3.2: Symmetry-independent atoms of the magnetic structure of $GdMn_2O_5$

Table 3.1 lists the symmetry operations that define the MSG for the magnetic structure of $GdMn_2O_5$. Each row contains operations in crystallographic notation, alongside the transformation of magnetic moments, with additional symbols for time reversal. The column labelled by N lists the symmetry operations on the coordinates

$$(x, y, z)$$

of the atoms in the crystal structure. It specifies how each point in space is transformed by different operations, e.g. reflections, translations and mirror symmetries. (m_x, m_y, m_z) column describes the transformation of a generic spin (m_x, m_y, m_z) associated with the general position (x, y, z). Seitz notation, a standard notation in crystallography that combines rotation and translation, is also provided, where for example {1 | 0, 0, 0 } is the identity operation (without any rotation or translation), while { m_{100} | 1/4, 1/2, 0 } indicates a mirror operation combined with a translation along a specific crystallographic directions. +1 and -1 eventually indicate whether the time-reversal

symmetry is respectively applied or not. Operations marked with the prime symbol involve time-reversal symmetry, which affects the a-magnetic moments by reversing their direction.

Table 3.2 provides a description of the symmetry independent atoms in the unit cell of $GdMn_2O_5$ and the components of their magnetic moments. First column refers to different atomic sites in the structure for the different gadolinium, manganese and oxygen atomic positions in the structure, while the atom type column says which type of atom is located at each site. x, y, and z columns specify the atomic coordinates of each atom within the unit cell, based on the basis ($2a_p$, b_p, c_p; 0, 0, 0) where a_p, b_p, c_p are the parent Pbam basis. M column represents the total magnitude of the magnetic moment for each atom, calculated using the components along x, y and z directions given in the following columns M_x, M_y, M_z, in which the components of the magnetic moments are expressed in terms of the Bohr magneton μ_B. These components are very useful since they give insights into the magnetic ordering of the material. For instance, Mn2_1 and Mn2_2 have identical moments, reflecting an important symmetry correlation between these sites.

This magnetic structure can be seen in Figure 3.1, where two twin configurations, whose different symmetries are described by the different but conjugated MSG indicated below.

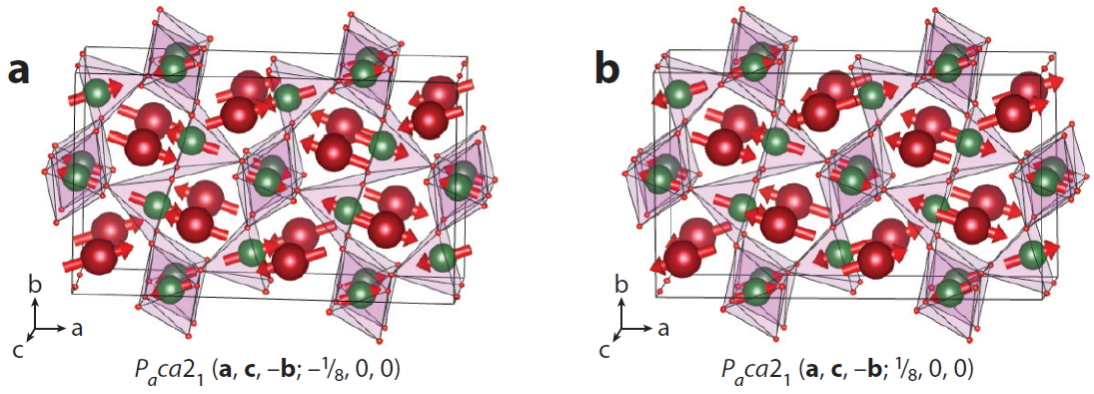

FIGURE 3.1: **a**: Magnetic structure of $GdMn_2O_5$ described in Tables 1 and 2. **b** Twin structure equivalent to panel **a**. The two configurations must have opposite, magnetically induced polarizations. Their symmetry is given by different but conjugate magnetic space groups indicated below.

What's more, Table 3.2 indicates that the spin model reported for $GdMn_2O_5$ has simplifying features that are not symmetry forced: the Mn1 moment is constrained to lie in the ab plane, whereas the spins of the two independent $Mn2_1$ and $Mn2_2$ sites are restricted to be exactly equal. Although these restrictions may be reasonable, it is important to have them clearly separated from the fundamental ones that are symmetry

protected (evidenced in Table 3.2). Lacking more precise details, the atomic positions listed in Table 3.2 are those of the paramagnetic phase and therefore comply with the parent space group Pbam (#55), but the table shows that some atomic sites are split because of the symmetry reduction. Hence, in principle, these split sites could vary their positions independently within the magnetic phase if magnetostructural couplings are sufficiently large. Also, the Mn1 site, which does not split, transforms into a general position, with its three coordinates becoming free. These new structural degrees of freedom are hints for possible structural distortion induced by the magnetic ordering: Table 3.1 gives the effective space group that governs their triggering with respect to the paramagnetic phase, disregarding the presence of time-reversal in the operation. Such space group is $Pmc2_1$ (#26), and its role is the one of the H group described above. Thus, magnetic ordering implies an effective symmetry breaking for the atomic positional structure: $Pbam \rightarrow Pmc2_1$ without change of lattice. This is a transformation from a nonpolar phase to a polar one (with the polar axis along the b direction of the parent setting), so, according to the von Neumann principle, an induced electric polarization P_b is expected.

Hence, the symmetry characterization of the magnetic structure of $GdMn_2O_5$ shows that the considered system behaves like a multiferroic of type II, with a magnetically induced ferroelectricity. This is all confirmed by the previously discussed experimental evidence.

3.4 Two AFM chains: $\mathbf{L}_1$ and $\mathbf{L}_2$

Once the structure and the symmetries of $GdMn_2O_5$ are explained, it is easier to analyze the correlation between the interactions within the unit cell, in order to identify the optimal order parameters to build a minimal Landau theory-based model.

As already mentioned in Chapter 2, the strong antiferromagnetic intrachain interactions between Mn^{4+} ions in octahedral coordination and Mn^{3+} ions in pentahedral coordination form zigzag chains along the crystallographic a-axis. The Néel vectors $\mathbf{L}_1$ and $\mathbf{L}_2$ are the antiferromagnetic order parameters corresponding to the magnetic moments' arrangement in these two distinct AFM zigzag chains. Antiferromagnetic coupling of Mn ions along these chains means that neighbouring spins are aligned in opposite directions, producing the nearest-neighbour intrachain interactions, denoted by $J_{||}$, which are significantly strong and dominating over the weaker interchain interactions, which are geometrically frustrated due to the formation of AFM pentagons involving Mn ions from neighbouring chains. Such geometric frustration leads to complex interactions, whose contribution to the system's ordered magnetic state is however much less relevant

than the one from intrachain interactions. When $\mathbf{L}_1$ and $\mathbf{L}_2$ of the two chains are non-collinear, i.e. not parallel, then the system experiences a significant energy gain due to the spin canting, that allows energy gains proportional to the canting angles, especially in the presence of interchain exchange interactions $J_\perp$. Competition between interchain and intrachain exchanges creates conditions under which the system stabilizes in configurations where the magnetic moments of the two chains are coupled but not aligned, thus reducing the overall energy. Also, the role of $\mathbf{L}_1$ and $\mathbf{L}_2$ is crucial because the coupling between these two magnetic order parameters is strongly linked to the electric polarization through the Heisenberg exchange striction mechanism. The two chains indeed contribute to the electric polarization along the crystallographic b-axis proportionally to $\mathbf{L}_1 \cdot \mathbf{L}_2$. This magnetoelectric coupling is an important feature among multiferroics like $GdMn_2O_5$, and is crucial for the overall behaviour of the system under the action of external fields. Hence, $\mathbf{L}_1$ and $\mathbf{L}_2$ play a central role for the topologically protected switching behaviour observed in $GdMn_2O_5$, since the system's transition between different magnetic configurations is strictly linked to interplay between these magnetic order parameters. Thus, it naturally comes that the two order parameters that have to be chosen for a minimal Landau theory model are indeed $\mathbf{L}_1$ and $\mathbf{L}_2$.

3.5 Analysis of the symmetry properties of the order parameters

To summarize the discussion above, the symmetry of the crystal and the anisotropy in the magnetic interactions restrict the form of the free energy to take into account for the interaction between the two chains by dominating terms that dictate the system's response to external fields. The possible coupling terms involve the products of the two order parameters $\mathbf{L}_1$ and $\mathbf{L}_2$ and either the induced electric polarization or the external field. To understand how these combination can be obtained, it is necessary to analyze once again the symmetry of the crystal, focusing on the behaviour of the two order parameters under the symmetry transformations allowed by the crystal's space group.

Recalling what has already been explained above, the crystal system is orthorombic, with a centrosymmetric lattice in P*bam* space group. "P" indicates a primitive Bravais lattice, thus there are lattice points only at the corners of the unit cell (that means no additional points inside the unit cell or on the faces). So, considering periodic boundary conditions, it has only one lattice point per unit cell. "*b*" denotes the presence of a glide plane along the b-axis (i.e. the y-direction in crystallographic coordinate system). A glide plane is symmetry operation that combines a mirror reflection and a translation by half of the unit cell along a specific direction, in this case the b-axis, along

which the crystal is then reflected and translated by 1/2 of the unit cell length. "a" indicates the presence of another glide plane, this time along the a-axis (x-direction in the crystallographic system), so it acts similarly to the one just discussed, but along a perpendicular direction. Finally, "m" represents the presence of a mirror plane parallel to the c-axis (z-direction). This is a symmetry operation that reflects the structure across mirror plane perpendicular to the c-axis. This specific combination of allowed operations described by Pbam space group determines the overall symmetry properties of the crystal structure, explaining how it repeats itself in three dimensions. Since the interaction terms in the free energy must be invariant under these operations, it is now necessary to analyze how these symmetry operations act on the parameters which are relevant for the construction of these terms. They are the two order parameters $\mathbf{L}_1$ and $\mathbf{L}_2$, the Cartesian components of the induced electric polarization P_x, P_y and P_z (even if the most relevant will result being P_b, that is P_y), and the two components of the external (magnetic) field in the xy plane, H_x, H_y. Table 3.3 shows how these quantities transform under the different generators of Pbam space group.

TABLE 3.3: **Transformation properties** of AFM order parameters, the induced polarization and the components of the external magnetic field under the Pbam space group symmetry operations.

Operation/Quantity	AFM Order Parameters				Polarization			$L_1 \cdot L_2$	Magnetic Field	
	L_{1x}	L_{1y}	L_{2x}	L_{2y}	P_x	P_y	P_z		H_x	H_y
Identity (E)	L_{1x}	L_{1y}	L_{2x}	L_{2y}	P_x	P_y	P_z	$L_1 \cdot L_2$	H_x	H_y
σ_x (x-mirror)	$-L_{1x}$	$-L_{1y}$	$-L_{2x}$	$-L_{2y}$	$-P_x$	P_y	$-P_z$	$L_1 \cdot L_2$	$-H_x$	H_y
σ_y (y-mirror)	L_{1x}	$-L_{1y}$	L_{2x}	$-L_{2y}$	P_x	$-P_y$	P_z	$-L_1 \cdot L_2$	H_x	$-H_y$
σ_z (z-mirror)	$-L_{1x}$	L_{1y}	$-L_{2x}$	L_{2y}	P_x	P_y	$-P_z$	$-L_1 \cdot L_2$	$-H_x$	H_y
Inversion (I)	$-L_{1x}$	$-L_{1y}$	$-L_{2x}$	$-L_{2y}$	$-P_x$	$-P_y$	$-P_z$	$L_1 \cdot L_2$	$-H_x$	$-H_y$

This table is built from the following rules given by Pbam generators:

1. Identity operation:
   - No changes are induced in any coordinate or vector component: $(x, y, z) \to (x, y, z)$
2. Two-fold rotations ($C2$) along the axes:
   - $C2$ along the x-axis (180° rotation): $(x, y, z) \to (x, -y, -z)$
   - $C2$ along the y-axis (180° rotation): $(x, y, z) \to (-x, y, -z)$
   - $C2$ along the z-axis (180° rotation): $(x, y, z) \to (-x, -y, z)$
3. Mirror planes (m):
   - Mirror plane perpendicular to x-axis (σ_x, yz-plane): $(x, y, z) \to (-x, y, z)$
   - Mirror plane perpendicular to y-axis (σ_y, xz-plane): $(x, y, z) \to (x, -y, z)$

- Mirror plane perpendicular to z-axis (σ_z, xy-plane): $(x, y, z) \rightarrow (x, y, -z)$

4. Glide planes:

   - a-glide along x-axis: $(x, y, z) \rightarrow (x + 1/2, -y, z)$
   - b-glide along y-axis: $(x, y, z) \rightarrow (x, y + 1/2, -z)$
   - c-glide along z-axis: $(x, y, z) \rightarrow (-x, y, z + 1/2)$

5. Inversion: $(x, y, z) \rightarrow (-x, -y, -z)$

From these, it is possible to build the following Landau free energy using invariant terms:

$$F = \gamma(\mathbf{L}_1 \cdot \mathbf{L}_2)^2 + \sum_{i=1,2} \left(k_2 \left(\mathbf{L}_i \cdot \mathbf{n}_i\right)^2 + k_4(\mathbf{L}_i \cdot \mathbf{n}_i)^4 + (\mathbf{L}_i \cdot \mathbf{H})^2 + \beta L_{ix} L_{iy} H_x H_y \right), \quad (3.1)$$

where the first term with the coefficient γ arises from the interaction between the AFM chains in the zigzag structure, that is, from the frustrated AFM pentagons, formed by interchain interactions $J_\perp$ connecting nearest neighbors on one AFM chain with the next nearest neighbors on the other one. When $\mathbf{L}_1$ is perpendicular to $\mathbf{L}_2$, the system minimizes the frustration between zigzag chains, resulting in energy gain. That is to say that when the AFM order parameters of the two chains are parallel, the energy gain on one of these $J_\perp$ interactions cancels the loss on the other one. However, if $\mathbf{L}_1 \perp \mathbf{L}_2$, spins can cant to produce the energy gains on these interactions, linear in the canting angles, while losing quadratically on the intrachain exchange $J_{||}$, thus leading to the overall energy gain $\gamma \propto {J_\perp}^2/J_{||}$. This will be very useful when it comes to the setting of the parameters in computational models. The terms with k_2 and k_4 represent the single-ion anisotropies in the system, respectively describing the quadratic and the quartic contributions, and being $\mathbf{n}_i$ the easy axes aligned with the axes of the bipyramids and the tetrahedra. The fourth term is the Zeeman energy gain on the spin canting when the AFM order is perpendicular to the external field. That is the interaction between the AFM order parameters and the external magnetic field, which lowers the energy of the system when they are aligned. The last term, the β term, is allowed by the symmetry of the P*bam* space group and couples the components of the AFM order parameters with the ones of the external magnetic field. It reflects the strongly anisotropic interaction between the field and the AFM vector, and because of this it is indeed expected to be very small and then negligible for the switching regime. This will also be useful for the computational choice of parameters of the model.

3.6 Computational reproduction of the switching behaviour

Through the just built Landau functional, it is possible to reproduce the switching behaviour observed in $GdMn_2O_5$ with great simplicity and clarity by computational simulations. The main goals that could be reached through the following simulations, since the generality of the Landau functional and the tunability of its parameters, are not only the reproduction of the experimentally observed behaviour, but also the potential further investigation for other (multiferroic) materials which allow topological switching effects. This is due to the fact that the ability to reproduce the topological effect obviously hinges on the particular values of model parameters, which determine different switching regime regions.

The simulations were conducted using Wolfram Mathematica Inc., n.d. (codes provided in the Appendix), and the prevalent computational method implemented was the Nudged Elastic Band (NEB) method and its optimizations, such as the Climbing Image NEB (CI-NEB), which are described in detail in Appendix A.

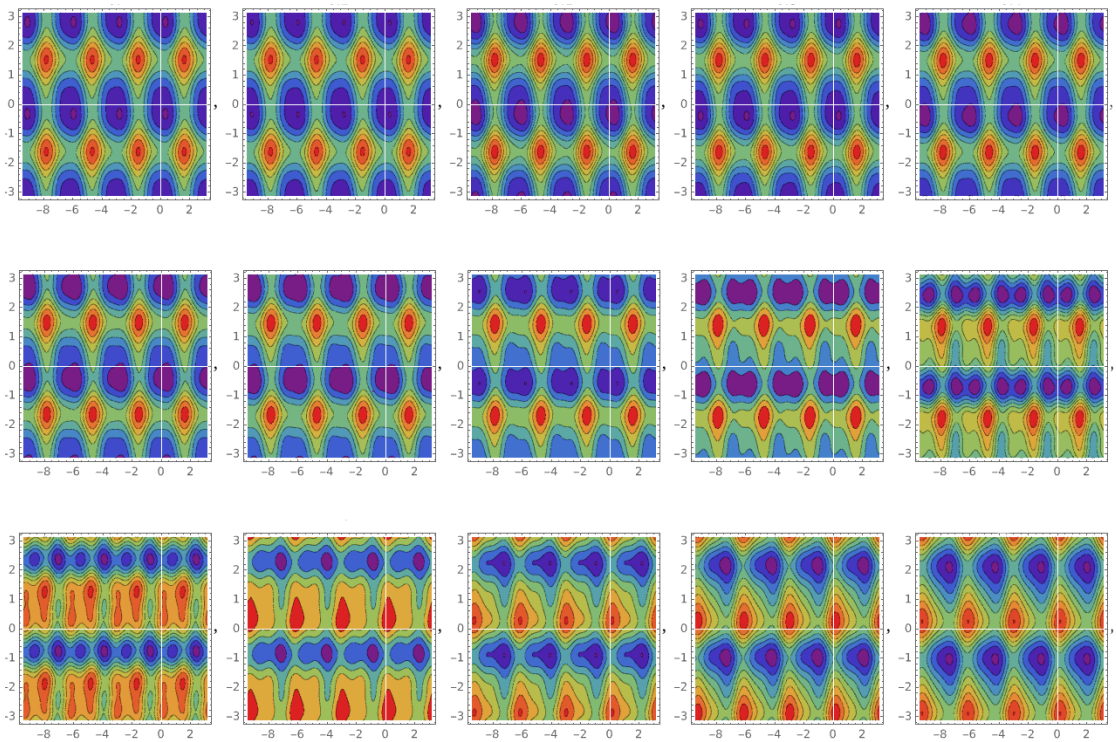

FIGURE 3.2: **Primeval attempt of tracking the evolution of the minima** in the PES landscape $F(\phi_1, \phi_2)$ using density plots. Presented here are several density plots for a trial set of parameters for our model: γ = 0.1, K_2 = -1, K_4 = 0.1, ϕ_H = 10°, β = 1, and the external magnetic field, in arbitrary units, goes from 0 to 1.4 (from upper left to lower right panel). x-axis represents ϕ_1 while y-axis represents ϕ_2 (both in radians). The scale goes from purple (minima) to red (maxima).

3.6.1 Tracking of the minima

Since the mentioned four states involved in the topologically protected switching correspond to four local minima of the Landau free energy, the main way to study this behaviour is to keep track of the evolution of these minima (i.e. the evolution of the barriers of PES) while varying model parameters and external conditions (that are the strength and orientation of the external fields). NEB method is then a really powerful tool, since it makes it possible to find the minimum energy path (MEP) between an initial and a final state (both local minima). Thus, once a topologically protected switching has been found for some parameter values, the switching can be observed in the evolution of PES barriers while ramping up and down the external magnetic field strength twice in the suitable range, while it is directed at an appropriate "magic angle" to the a-axis. Once parameters are initialized, somehow taking inspiration from the experimental orders of magnitude and from the considerations in Section 3.5, one can find the appropriate magnetic field interval by studying when PES barriers have either two or four local minima. In the first case, we are in the trivial switching situation between two states, while in the second case we can potentially have the topological switching among four states (accordingly to what is described in Chapter 2). As it will be more clear by just looking at the plots, and also explained in detail in the following, once the right parameter values are chosen, the evolution of the barriers with magnetic field sweeps (Fig. 2.3g) shows how the state is guided from the first minima to second, then from the second to the third, then from the third to the fourth and finally from the fourth to the first again by raising up and lowering down external field twice. Figure 3.3 illustrates a primordial attempt of this method, that will be highly improved in Chapter 4, where clearer plots are presented.

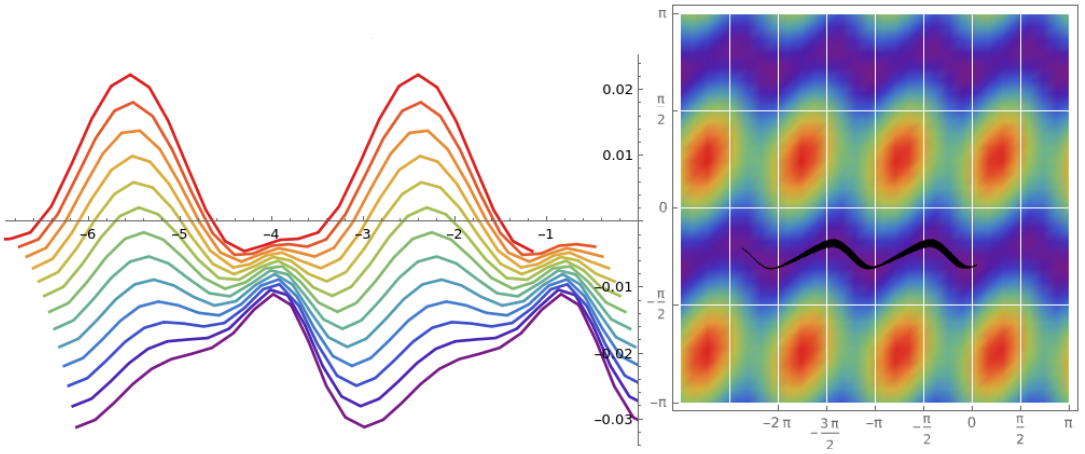

FIGURE 3.3: **Preliminary attempt of studying barriers evolution** of the PES (on the left), while on the right it shown the corresponding density plot for the first value of magnetic field. Black line is the MEP obtained through NEB method. The naive set of parameters was: $\gamma = 0.07$, $K_2 = -1$, $K_4 = 0.1$, $\phi_H = 15°$, $\beta = 0$, and the external magnetic field, in arbitrary units, goes from 0 to 0.6 with steps of 0.05 (from purple barrier corresponding to 0, to red barrier corresponding to 0.6). On the x-axis is ϕ_1. For the density plot on the right, x-axis represents ϕ_1 while y-axis represents ϕ_2 (both in radians)

Thus, one could potentially already say that our phenomenological model is reproducing the topologically protected switching between the four states. What's more is that one can also get the same plot displayed in Figures 2.2 and 2.5 b, for the topological switching seen through the induced electric polarization, where it is shown how the ramping of the field does not simply invert the polarization along b-axis between positive and negative values for each sweep, but instead it creates a topological switching for the polarization that is positive in the first two states and negative in the last two. So, instead of having a positive → negative → positive → negative transition for the polarization as in the trivial switching situation, we have a positive → positive → negative → negative topological switching. This will be detailed in Section 3.4.

3.7 Polarization and parameter tunability

An additional kind of plot, that can be obtained from these simulations, is the highly informative ϕ_H angle-dependent switching regime diagram of $GdMn_2O_5$, that basically displays how the induced polarization $P_b(H, \phi_H)$ changes through H sweeps as a function of the magnetic field direction, ϕ_H. Its advantage is double: on one hand, it enables a direct comparison with experimental data, and, on the other hand, it allows to perceive how the tunability of the Landau theory parameters creates different possible regions that give rise to the switching regime, whose width is strongly dependent on them.

Figure 3.4 displays experimental data obtained by our collaborators in Prof. Dr. Pimenov's group (Institut für Festkörperphysik, TU Wien, Austria). They measured the polarization of a sample of $GdMn_2O_5$ at different field angles ϕ_H to the a-axis (while ramping up and down the intensity of the magnetic field). The polarization switching between positive and negative values can be clearly observed. It goes in the trivial way for the central region, while in the topological way for the two outside regions, that exist roughly in the ϕ_H intervals between 6° and 11° (and between -6° and -11°), approximately.

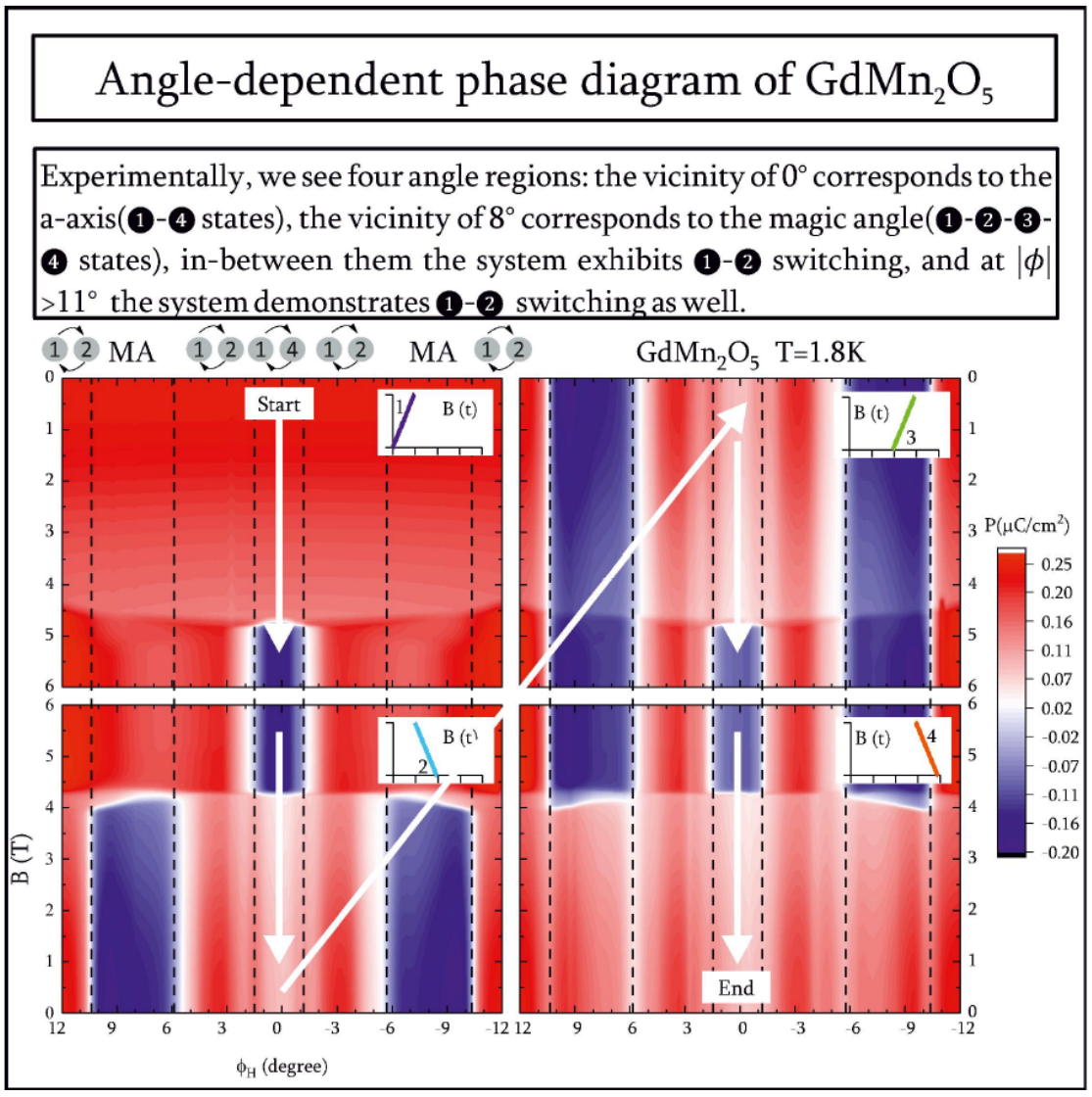

FIGURE 3.4: **Experimental data** obtained by Prof. Dr. Pimenov's group (Institut für Festkörperphysik, TU Wien, Austria)

Our simulations can reproduce qualitatively almost analogous plots, even though certain differences still require further in-depth analysis. The two main differences are the

presence of a gap with always positive polarization between the standard and the topological switching regions, and the width of these regions. In our first simulations this gap, where the polarization is always positive, is indeed missing, and, most of all, the magic angle interval is much thinner than the angle interval where the trivial switching takes place. Nonetheless, the plots are still useful to gain an insight into the topological switching regime regions, especially about the magic angle intervals. It seems in fact that the width of this interval can be widened or thinned by manipulating the free energy parameters. Also, the plots indicate how the sign of the quartic anisotropy term k_4 is responsible for getting a positive → positive → negative → negative polarization switching or a negative → negative → positive → positive switching, depending on whether it is negative or positive respectively. Table 3.4 indicates the values used for a subset of our simulations, that are presented in Figures 3.5, A-F.

Parameter set N	K_2 $[(\mathbf{L}_i \cdot \mathbf{n}_i)^2]$	γ $[(\mathbf{L}_1 \cdot \mathbf{L}_2)^2]$	K_4 $[(\mathbf{L}_i \cdot \mathbf{n}_i)^4]$	β $[(L_{1x}L_{1y} + L_{2x}L_{2y})H_xH_y]$
1	-1	0.076	-0.1	$5{\cdot}10^{-5}$
2	-1	0.076	+0.2	$5{\cdot}10^{-5}$
3	-1	0.076	-0.1	$5{\cdot}10^{-5}$
4	-1	3·0.076	-0.2	$5{\cdot}10^{-5}$
5	-1	3·0.076	-0.1	$5{\cdot}10^{-5}$
6	-1	7·0.076	-0.2	$5{\cdot}10^{-5}$

TABLE 3.4: **Sets of parameters** used for the different switching phase diagrams reported in Figure 3.5

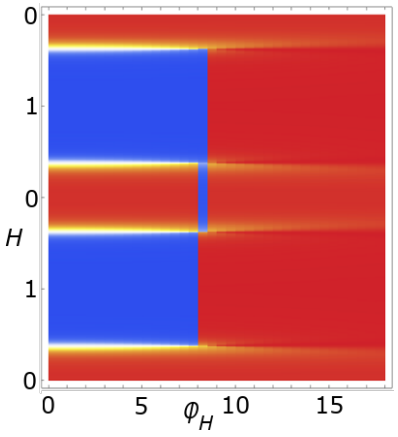

(A) Parameter set 1

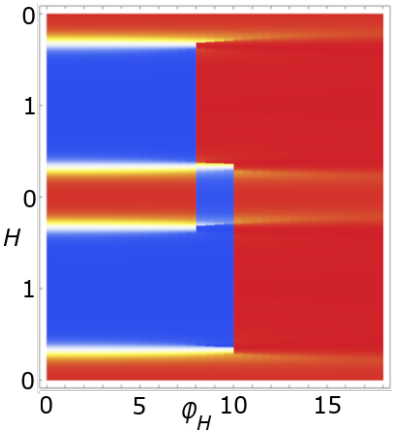

(B) Parameter set 2

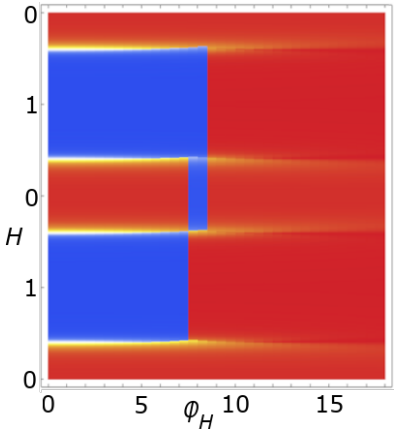

(C) Parameter set 3

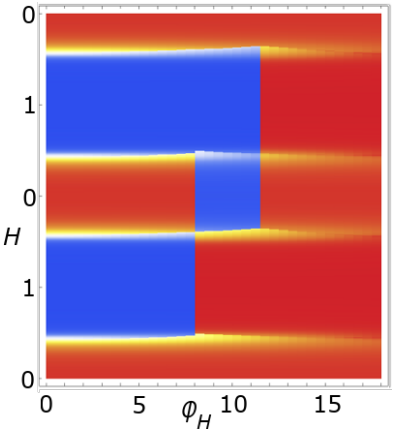

(D) Parameter set 4

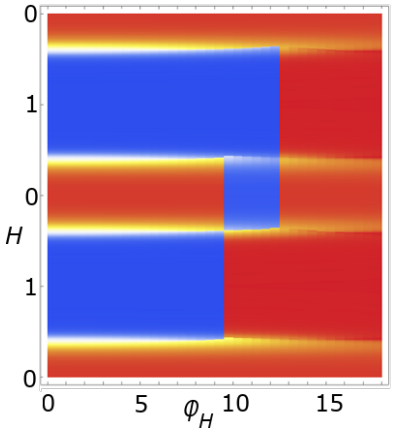

(E) Parameter set 5

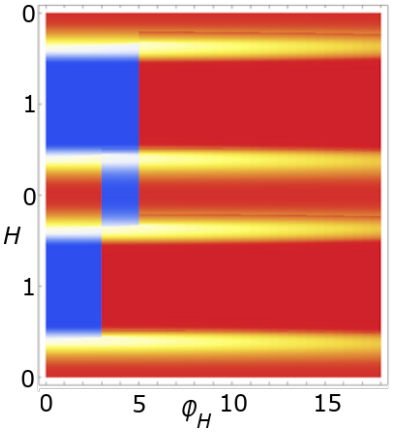

(F) Parameter set 6

FIGURE 3.5: Color plots illustrate the evolution of $P_b(H)$ during field sweeps (vertical cuts) for different magnetic field orientations ϕ_H (on the horizontal axis). Areas with positive polarization P_b are in red, negative – in blue. The evolution of the magnetic field strength during sweeps is marked on the y axis (time is going from the bottom to the top).

Chapter 4

Electric field control of the topological switching

4.1 Anticipated developments and implications

The work conducted thus far naturally leads to further opportunities, both including a wider spectrum of the explored physics and driving towards remarkable technological potential. Instinctively, one could indeed add an extra term to our free energy, representing the interaction of the magnetically induced polarization $P_b \sim \mathbf{L}_1 \cdot \mathbf{L}_2$ with an external electric field component along the crystallographic b-axis. Hence, our Landau free energy becomes

$$\begin{aligned} F = & \ \gamma(\mathbf{L}_1 \cdot \mathbf{L}_2)^2 - \alpha E_b \mathbf{L}_1 \cdot \mathbf{L}_2 \quad + \\ & + \sum_{i=1,2} \left(k_2 \left(\mathbf{L}_i \cdot \mathbf{n}_i\right)^2 + k_4 (\mathbf{L}_i \cdot \mathbf{n}_i)^4 + (\mathbf{L}_i \cdot \mathbf{H})^2 + \beta L_{ix} L_{iy} H_x H_y \right), \end{aligned} \tag{4.1}$$

where α is a constant that is added to keep the normalization of the polarization coherent with experimental results, and in our case has been chosen to be $\alpha = 0.155$. Other parameters are chosen to be coherent with Figure 4.4, as it will be soon explained. They are $\gamma = 0.076$, K_2 =-1, K_4 =-0.01, $\beta = 5{*}10^{-5}$, $\phi_H = +8°$. The positive sign of ϕ_H simply means that the order parameter that will be affected by the magnetic field, producing the topological switching, is $\mathbf{L}_1$. Then the state transition will be tracked by the variation of ϕ_1.

It is now straightforward to see what happens when adding this electric field term, while keeping all of the background configuration in a suitable switching regime, that

would give us the topological switching seen without an external electric field. The magnetic external field is ramped in an optimal range of values for the switching, and its orientation with respect to the crystallographic a-axis belongs to the magic angle region.

The effects of the external electric field can be observed in Figure 4.1.

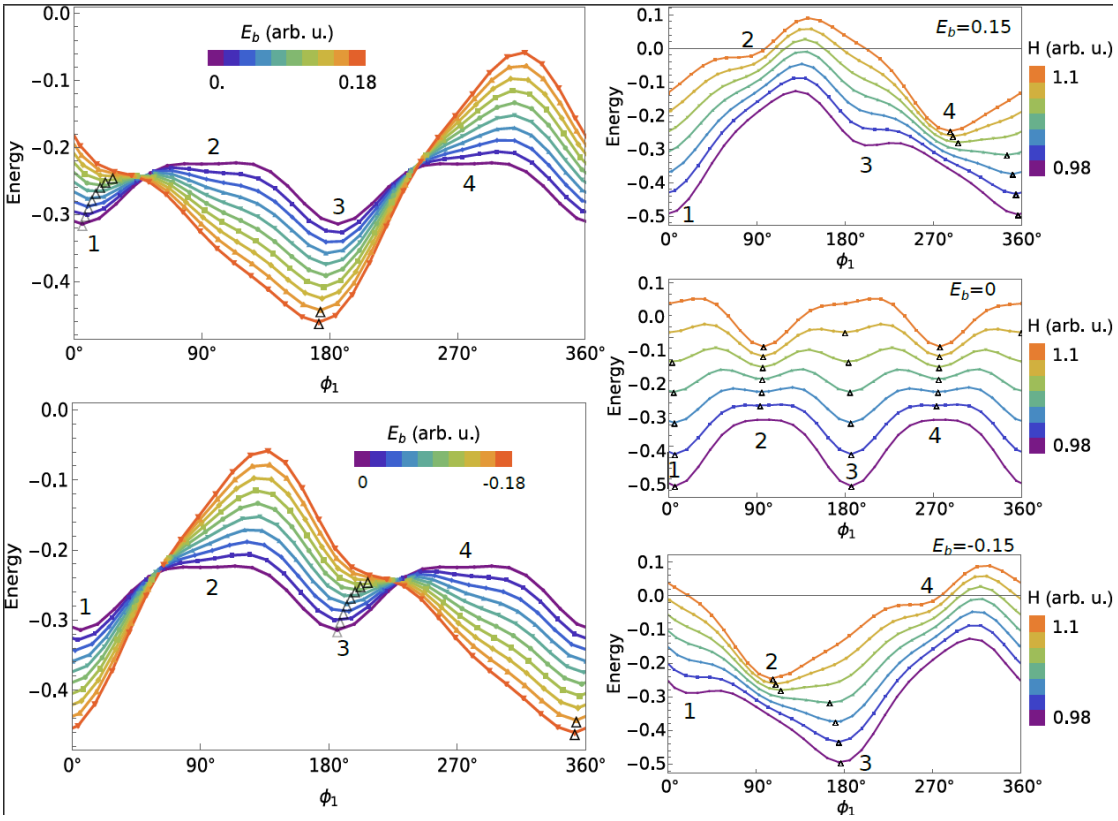

FIGURE 4.1: **NEB simulation of barrier evolution for the system under different conditions.** Landau free energy parameters are $\gamma = 0.076$, K_2 =-1, K_4 =-0.01, $\beta = 5 \cdot 10^{-5}$, $\alpha = 0.155$, $\phi_H = +8°$. **First column**: H = 1 (arb. u.), **upper plot**: E_b goes from 0 to 0.18 (arb. u.), switching $1 \rightarrow 3$; **lower plot**: H = 1 (arb. u.), E_b goes from 0 to -0.18 (arb. u.), switching $3 \rightarrow 1$. **Second column**: **upper plot**: E_b is fixed at 0.15 (arb. u.), H is ramping between 0.98 and 1.1 (arb. u.), switching $1 \rightarrow 4$; **middle plot**: E_b is fixed at 0, H is swept between 0.98 and 1.1 (arb. u.), topological switching between all the four states: $1 \rightarrow 2 \rightarrow 3 \rightarrow 4$; **lower plot**: E_b is fixed at -0.15 (arb. u.), H is ramped between 0.98 and 1.1 (arb. u.), switching $3 \rightarrow 2$.

The second column in Figure 4.1 depicts three different situations, which illustrate the evolution of the potential energy landscape in the three cases. The middle plot simply displays the topological switching seen without the electric field, with the state transition described in Chapter—2, coherently with **g** panel in Figure 2.3. The upper and lower plots start from the same configuration but they are affected by positive and negative external electric fields respectively. It is evident how the shapes of potential barriers are modified so strongly to the extent that the topological switching between all the four

states is no longer possible, breaking up into two different switching paths between only two states each. For a positive electric field, the switching is between states 1 and 4, while for a negative electric field the switching between states 2 and 3 occurs.

First column of Figure 4.1 focuses instead on what happens when the system is subjected to the magnetic field strength near the switching value (so, in this case and with these units, $H = 1$), and then a positive/negative electric field is ramped up from zero to a boundary value, leading to the PES evolution in the upper/lower plots of Fig. 4.1(left). This first column shows now a different transition: between states $1 \rightarrow 3$ when the electric field is positive, and $3 \rightarrow 1$ when electric field is negative.

Hence, it is lucid how the transition between different states of the system is deeply influenced by the presence of the external electric field, opening the door to electric control of the switching.

Further investigations are then required, driven by some vital questions: how far can we push this electric control? Are some peculiar parameters of the system mandatory? Is orienting the magnetic field near a magic angle, crucial for the topological switching without electric field, still necessary?

4.2 Experimental results

To effectively respond to the inquiries from the previous section and to conduct additional investigations, a collaboration with the experimental group of Prof. Dr. Pimenov (Institut für Festkörperphysik, TU Wien, Austria) has been fundamental.

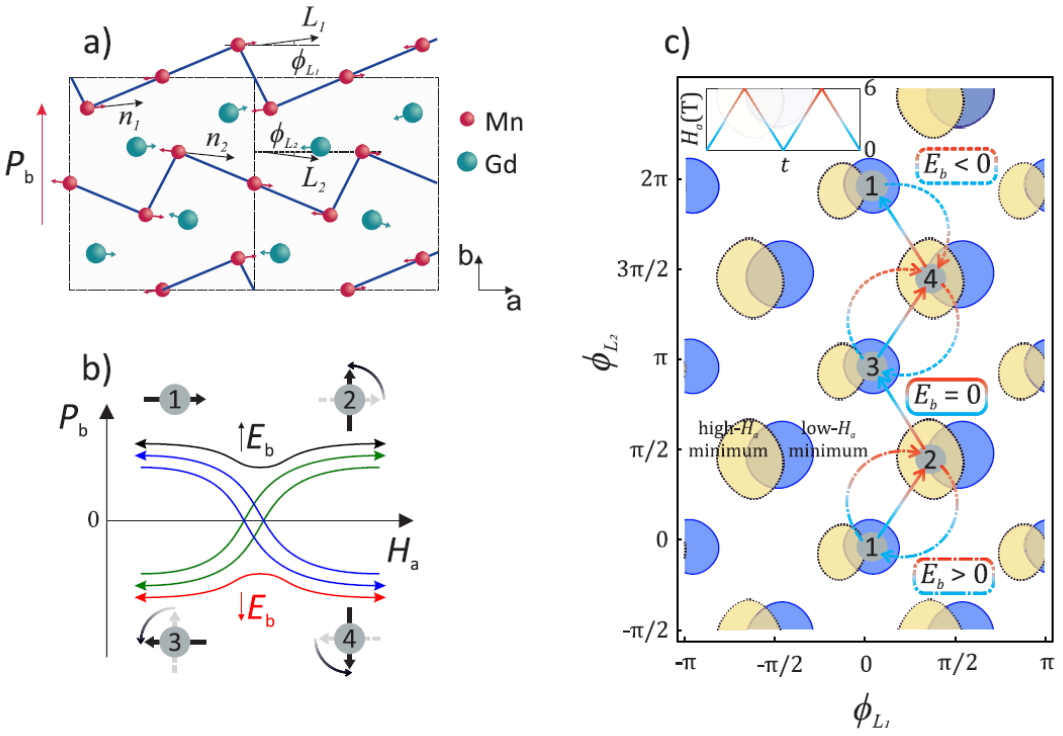

FIGURE 4.2: **Comprehensive scheme of the investigation**. **a**: Magnetic unit cell of $GdMn_2O_5$. Mn ions (red spheres) form zigzag chains (blue lines) along the a-axis with antiferromagnetic intrachain interactions between Mn spins. $\mathbf{L}_1$ and $\mathbf{L}_2$ are the Néel vectors for the two distinct chains. The easy axes for both chains are denoted as $\mathbf{n}_1$ and $\mathbf{n}_2$. Gd ions (dark cyan spheres) are inside the pentagons formed by Mn ions from the neighboring chains. The boundary of the structural unit cell is marked by the black dotted box. **b**: Schematic demonstration of a magnetoelectric switching with an applied constant positive or negative electric field during the magnetic field sweep. Depending on the direction of the electric field, the resulting polarization can be controlled and the system could be forced to any single unit state. **c**: Schematic energy landscape in space of angles between a-axis and $\mathbf{L}_1$, $\mathbf{L}_2$ vectors. At low (high) magnetic fields yellow (blue) puddles correspond to local minima. Solid arrows correspond to magnetic field sweeps along magic angle without E-field applied, dotted arrows are for negative E-field and $|\phi| < \phi_H^*$, dashdotted ones are for positive E-field and for $|\phi| < \phi_H^*$ as well. Each sweep start from state 1

Figure 4.2 displays a general idea of the work the experimentalists conducted and that we managed to explain through our minimal Landau model.

4.2.1 Control of magnetoelectric switching by electric field

The key experimental finding is that the application of external electric fields can modify and control this switching behavior. It is observed that for magnetic fields close to the *a*-axis, applying moderate electric fields ($E \sim 500\text{V/mm}$) can alter the switching sequence and influence the order of the states. This observation suggests that the electric field

plays a crucial role in guiding the system towards specific states, acting as a "push" that can overcome energy barriers and direct the switching pathway.

4.2.2 Electric field-driven switching sequence

The experiments demonstrate that various switching sequences could be achieved by applying positive or negative voltages, highlighting the controllability of the switching process. Specifically, the following individual switching events are observed:

- From state 1 to state 2 with positive voltage and to state 4 with negative voltage.
- From state 2 to state 1 with positive voltage and to state 3 with negative voltage.
- From state 3 to state 2 with positive voltage and to state 4 with negative voltage.
- From state 4 to state 3 with positive voltage and to state 1 with negative voltage.

By combining these individual steps, both clockwise (1-2-3-4-1) and counter-clockwise (1-4-3-2-1) four-state switching cycles were successfully realized. This achievement is significant because it replicates the previously observed cycles at magic H tilting angles, but now using electric fields instead of specific magnetic field orientations. Figure 4.3 illustrates these experimental results.

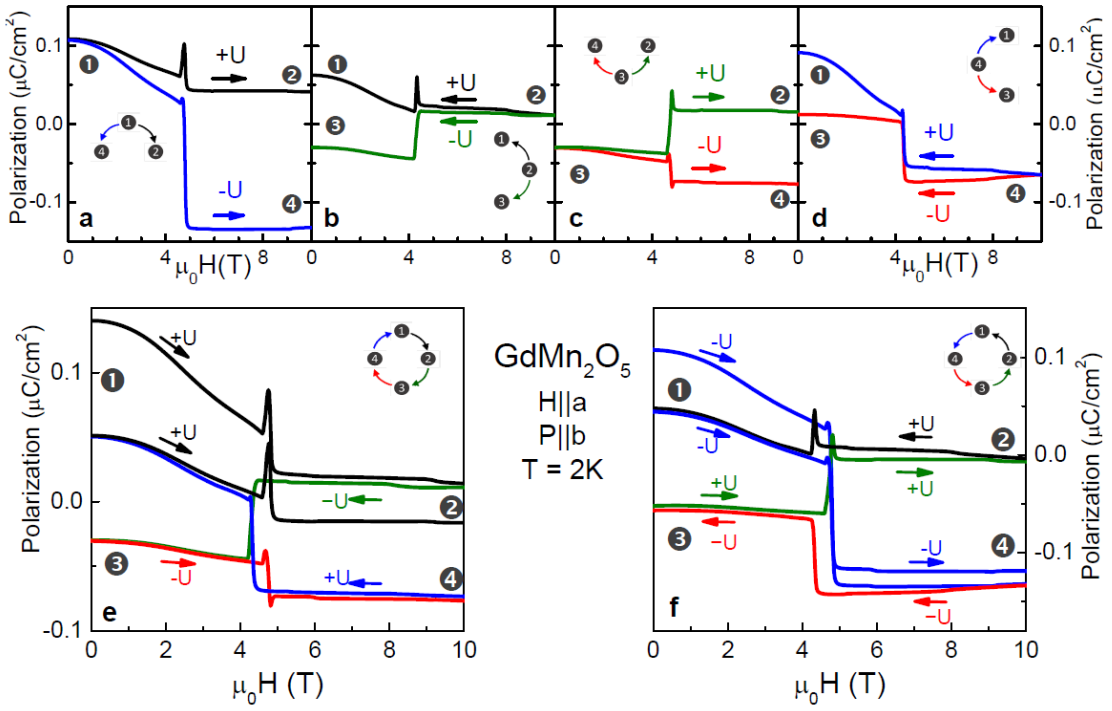

FIGURE 4.3: **E-field switching of magnetoelectric states** in $GdMn_2O_5$. **a-d**: E-field controlled switching between single unit states of the system. **a**: Switching from state 1 to states 2 and 4 at positive and negative applied voltage, respectively. **b**: Switching from state 2 to states 1 and 3. **c**: Switching from state 3 to states 2 and 4. **d**: Switching from state 4 to states 3 and 1. **e,f**: Combined four-state switching sequence with winding controlled through external electric fields: **e**: clockwise cycle 1-2-3-4-1. **f**: anti-clockwise cycle 1-4-3-2-1. Magnetic field is applied parallel to the a-axis (nominal deviation ˜1°)

4.2.3 Further considerations

- **Multidomain effects:**

  The authors of the experiments noted that the measured polarization state 2 differs from the expected monodomain state. The observed state 2 exhibited a polarization value closer to zero than anticipated. This observation was attributed to the presence of domains with opposing polarizations within the sample, influencing the overall polarization measurement.

- **Quantifying the electric field influence**

  To precisely quantify the effects of the applied electric field, the experiments were performed with an electric field of 380V/mm. They accounted for the induced polarization due to dielectric permittivity, $P_{b,ind} = \epsilon_0 \chi E$, and subtracted it from the measured values. Here, ϵ_0 represents the permittivity of vacuum and χ is the electric susceptibility of the material, which was measured as 17 ± 2. This

correction was crucial for accurately interpreting the influence of the electric field on the switching behavior.

- **Strain inhomogeneity effects:**
  It is also been acknowledged that strain inhomogeneity induced by the magnetic field could affect the reorientation transition field. The ionic displacements caused by strain can modify the magnetic exchange and anisotropy constants. This leads to variations in the transition field across the sample, impacting the overall switching behavior.

4.2.4 First theoretical model

We managed to reproduce the observed behaviour using the minimal Landau model Ryzhkov et al., 2024, with the result displayed in Figure 4.4.

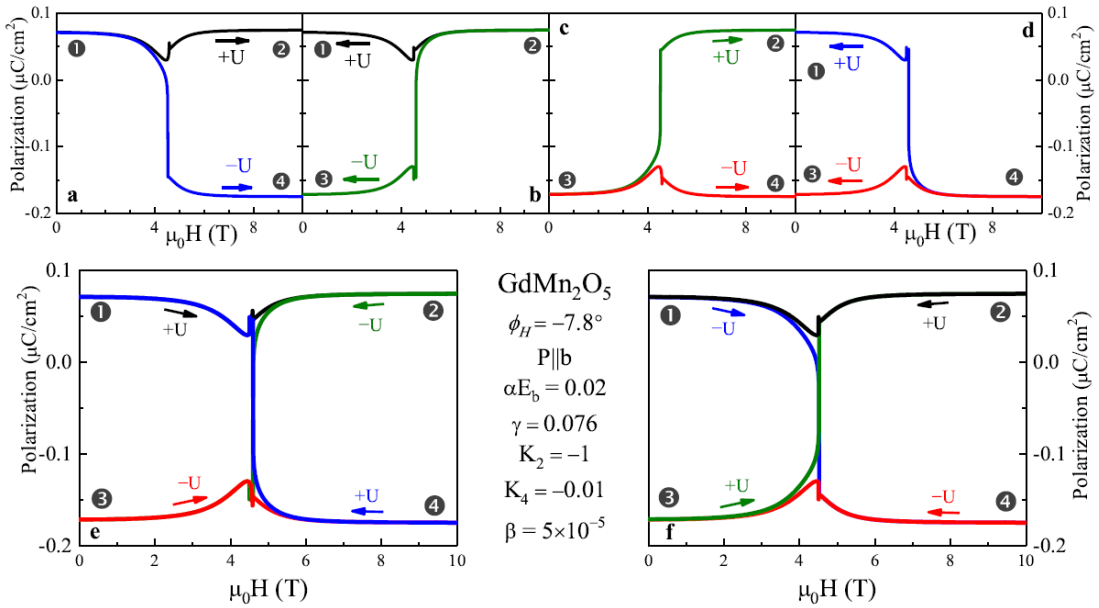

FIGURE 4.4: **Simulation of E-field controlled switching of magnetoelectric states in $GdMn_2O_5$ within the Landau model**. **a-d**: E-field controlled switching between individual states of the system. **a**: Switching from state 1 to states 2 and 4 at positive and negative applied voltage, respectively. **b**: Switching from state 2 to states 1 and 3. **c**: Switching from state 3 to states 2 and 4. **d**: Switching from state 4 to states 3 and 1. **e,f**: Combined four-state switching sequence with winding controlled through external electric fields: **e**: clockwise cycle 1-2-3-4-1. **f**: anti-clockwise cycle 1-4-3-2-1. Magnetic field is applied along $\phi_H = -7.8°$. $K_2 > 0$.

These results properly confirm the compatibility between experimental observations and the Landau model simulations, highlighting the significant control offered by electric fields over the magnetoelectric switching in $GdMn_2O_5$ even outside the magic angle

region, since the magnetic field has been directed at $\phi_H = -7.8°$, which is slightly outside the region for the used parameters and magnetic field range.

Nevertheless, a certain kind of incompleteness is still present. In fact, even though this simulation uses an angle outside the magic angle region, it is still very near to that interval, and then clearly a transition can be obtained even with a small perturbation from an external field. Hence, continued studies are essential.

4.3 Theoretical model implementation

First of all, with the aim of being consistent with experimental values, it is necessary to renormalize our free Landau energy, in order to get the switching value for the magnetic field at $H \simeq 5T$ (instead of H = 1 in our previously used arbitrary units). This leads to a multiplication by a factor of 25 for all the parameters described in Section 4.1 and used for Figure 4.1 (and also 4.4). Thus, now they become $\gamma = 1.9$, K_2 =-25, K_4 =-0.25, $\beta = 1.25 \cdot 10^{-3}$, α =3.875, $\phi_H = -4°$.

The second step is to study the evolution of the magic angle region exploiting the phase diagrams introduced in Section 3.7, ramping up and down the magnetic field strength in an interval surrounding the switching value while simultaneously applying electric fields, varying both the magnitude and the sign.

The results are presented in Figure 4.5. It is manifest how applying an external electric field allows to shift, or, more accurately, to shrink, the magic angle region to a more compact interval. This potentially permits an explanation of the smaller field angle ϕ_H used in the experiments, which is so minimal that the applied magnetic field is nearly parallel to the a-axis.

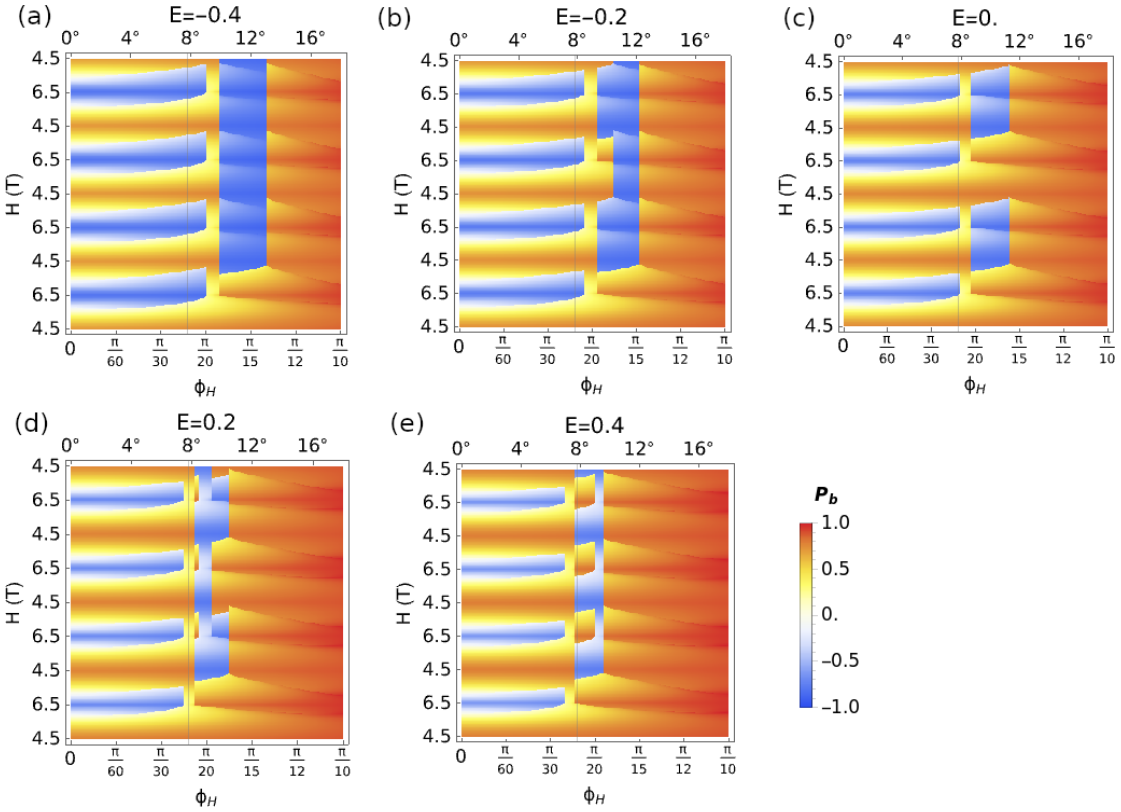

FIGURE 4.5: **Evolution of magnetically induced polarization P_b during magnetic field sweeps under different values of an external electric field.** Every vertical cut corresponding to ϕ_H shows $P_b(H, E)$ when H is directed at the angle ϕ_H to the a-axis and swept up and down. The E_b values are given above the plots. All the five diagrams show the behaviour of polarization P_b of the system with Landau free energy parameters $\gamma = 1.9$, K_2 =-25, K_4 =-0.25, $\beta = 1.25 \cdot 10^{-3}$, α =3.875, $\phi_H = -4°$, $\phi_1^{(0)} = +6°$, $\phi_2^{(0)} = -6°$ when the external magnetic field is ramped up and down twice between 0 and 5 T, at different intensities for the applied electric field. Blue areas indicate negative polarization, while red areas – the positive one. First kind of switching on the left of each panel is the trivial switching $1 \to 4$, which is separated by a gap of positive polarization from the region of topological switching that gives negative - negative -positive - positive transitions. Despite strange effects that should be analyzed more thoroughly, it is evident how the magic angle region for the topological switching can be shifted or narrowed depending on the applied external electric field. From the first to the fifth diagram, the electric fields applied (in kV/cm) are respectively -0.4, -0.2, 0, +0.2, +0.4.

Building on this, we performed new simulations (similarly to the ones illustrated in Figure 4.1), using the new parameters (as in simulations shown in Figure 4.1, but multiplied by 25), the new magnetic field intensity range (enclosing the experimental switching value $H \sim 5$ T) and, notably, a much smaller angle for the direction of the external magnetic field, $-4°$. Note that the negative sign of ϕ_H only means that we are switching $\mathbf{L}_2$ spins, thus the transition between different states will be tracked by the variation of ϕ_2 angle. In the simulations illustrated in Figure 4.5 the switching $1 \to 2$ at low field angle is not achieved. Therefore, to better match the experiment, we further used significantly higher electric field intensities. The results are shown in Figure 4.6.

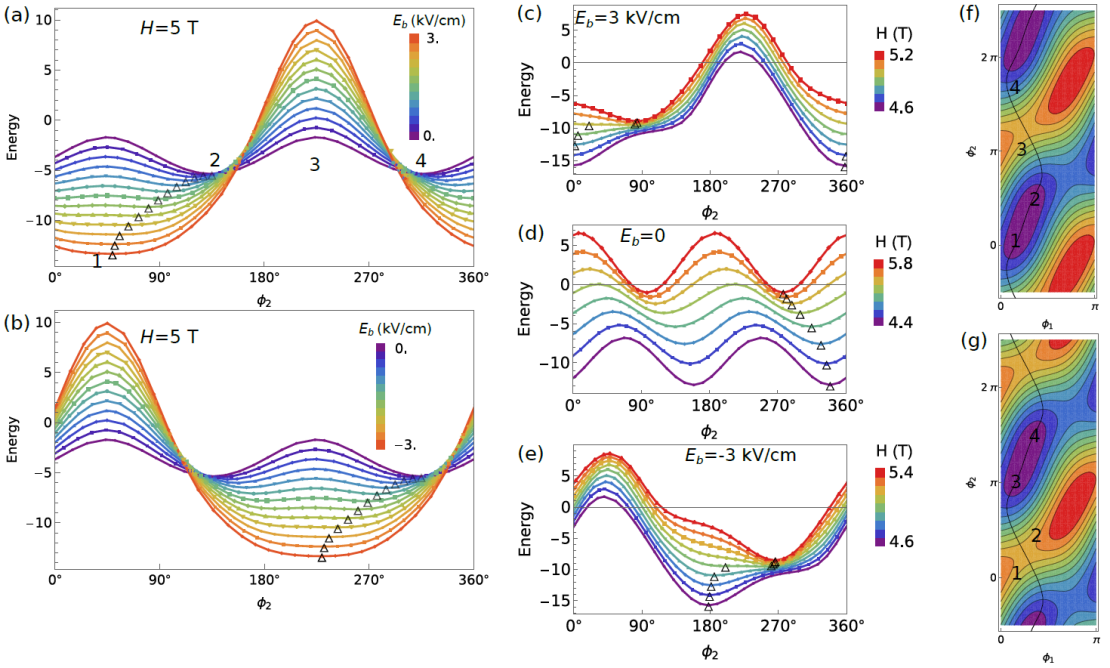

FIGURE 4.6: **NEB simulation of barriers evolution for the system in different conditions.** Landau free energy parameters are γ = 25*(0.076), K_2 =25*(-1), K_4 =25*(-0.01), β = 25*(5*10^{-5}) , α =25*0.155, ϕ_H = -4°, ϕ_1 = +6° , ϕ_2 = -6°. **a**: H = 5T, E_b goes from 0 to 3 kV/cm, switching 2 → 1. **b**: H = 5T, E_b goes from 0 to -3 kV/cm, switching 1 → 4. **c**: E_b is fixed at 3 kv/cm, H is ramping between 4.6 and 5.2 T, switching 1 → 2. **d**: E_b is fixed at 0, H is ramping between 4.4 and 5.8 T, switching 1 → 4. **e**: E_b is fixed at -3 kv/cm, H is ramping between 4.6 and 5.4 T, switching 3 → 4. **f,g**: density plots with same parameters as, respectively, **c** and **e**.

These simulations are now reproducing the experimental observations with significant consistency. The first column, analogous to the first column in Figure 4.1, shows the two possible switching steps from state 2 → 1 (or 1 → 4) when a positive (negative) electric field is applied, reproducing the phenomena taking place in panels **b** and **a** in Figure 4.3 and are still coherent with Figure 4.4 (again, panels b and a). In this case, the magnetic field is fixed at a certain value, but, since it is approximately at the switching value, it provides a proper description. Second column (panels c and e respectively) is showing how a fixed positive or negative external electric field modifies barrier evolution for the system subjected to the external magnetic field sweeping up and down around the switching value. Starting point is represented in panel d, where no electric field is applied and the only possible transition is between states 1 and 4. Thanks to the positive electric field, the switching becomes between states 1 and 2, while for negative electric field, it becomes between 3 and 4. This remarkably demonstrates how our minimal Landau model is able to describe transition among all the four states of the system, enabling a switching that does not require a precise direction for the external magnetic field, paving the way to a more accessible technological implementation. Third column in Fig. 4.6, which was not present in Figure 4.1, shows density plots of the potential

energy surface for the situations described in panel c for the plot f, and in panel e for plot g, including the illustration of the minimum energy path (MEP), obtained by NEB method, connecting initial and final states.

Chapter 5

Results and conclusions

To draw the conclusions of this work and highlight the interesting results, both from the perspective of the physics explored and the potential technological opportunities that appear accessible, it is necessary to recall how the topologically protected switching that has been analyzed is an extremely robust and potentially generalizable phenomenon. These characteristics are indeed the reason that inspired and necessitated this research. The technological potential that this topological switching offers, replacing the traditional extremely energy-intensive ferroelectric switching, opens the door to a path toward a much more efficient, robust, and functional technology, meeting both the urgency for energy optimization of global consumption in the coming years and the need for new means for technological progress, especially in the domain of data storage and analysis, a globally significant sector that is exponentially increasing.
However, it is chiefly the physics governing this phenomenon that's at the heart of the research. Topological effects like these are a territory still too unexplored, and in-depth analyses of these phenomena offer an ever closer yet simultaneously more distant view of the reality of matter.

5.1 Minimal Landau model

Inspired by the pursuit of elegance and simplicity, a generalization was the first thing we searched for. This is indeed the starting point of our analysis: to begin with a specific case, a single effect observed in a specific system, and attempt to generalize it using the symmetries and fundamentals of the material, with the hope of building a tool that allows for the discovery of analogous phenomena in other materials. Unfortunately, we have not yet succeeded in achieving this goal, as such a generalization still requires a lot of theoretical analysis and crystallographic database work. Nevertheless, we have made

a first step in this direction, namely, generalizing the original model, that contained a multitude of interactions, to a simplified "toy" model.
Starting from the complicated Hamiltonian proposed in the original article,

$$\begin{aligned}
H = &\gamma(\mathbf{L}_1 \cdot \mathbf{L}_2)^2 + \sum_a \chi\left((\mathbf{H} \cdot \mathbf{L}_a)^2 - H^2\right) + \\
&- K_L \sum_a (\mathbf{L}_a \cdot \mathbf{n}_a{}^2 - \sum_i (K_S(\mathbf{N}_i \cdot \mathbf{S}_i)^2 + g\mu_B \mathbf{H} \cdot \mathbf{S}_i) + \\
&+ \frac{1}{2}(g\mu_B)^2 \sum_{i \neq j} \left(\frac{\mathbf{S}_i \cdot \mathbf{S}_j}{r_{ij}^3} - 3\frac{(\mathbf{S}_i \cdot \mathbf{r}_{ij})(\mathbf{S}_j \cdot \mathbf{r}_{ij})}{r_{ij}^5} \right) + \\
&+ \sum_{i,\alpha} V_{i\alpha} \mathbf{S}_i \cdot \mathbf{L}_\alpha + \\
&- P_b[8\beta_1(\mathbf{L}_1 \cdot \mathbf{L}_2) + (\mathbf{S}_1 - \mathbf{S}_5)(\beta_2 \mathbf{L}_2 + \beta_3 \mathbf{L}_1) + \\
&+ (\mathbf{S}_2 - \mathbf{S}_6)(\beta_2 \mathbf{L}_1 + \beta_3 \mathbf{L}_2) + \\
&+ (\mathbf{S}_3 - \mathbf{S}_7)(\beta_2 \mathbf{L}_2 + \beta_3 \mathbf{L}_1) + \\
&+ (\mathbf{S}_4 - \mathbf{S}_8)(\beta_2 \mathbf{L}_1 + \beta_3 \mathbf{L}_2)] + P_b^2/2
\end{aligned} \tag{5.1}$$

and using symmetry arguments and Landau theory, we managed to construct a Landau free energy using the invariants of the system under the transformations allowed by its geometry (i.e., by the space group that describes it), resulting in a clearly much simpler expression:

$$F = \gamma(\mathbf{L}_1 \cdot \mathbf{L}_2)^2 + \sum_{i=1,2} \left(k_2 (\mathbf{L}_i \cdot \mathbf{n}_i)^2 + k_4 (\mathbf{L}_i \cdot \mathbf{n}_i)^4 + (\mathbf{L}_i \cdot \mathbf{H})^2 + \beta L_{ix} L_{iy} H_x H_y \right) \tag{5.2}$$

Thus, we constructed a minimal Landau model, with which we not only managed to reproduce the topologically protected switching observed in $GdMn_2O_5$, but, more importantly, we sketched a model that allows recreating the same phenomenon for different system parameters, bringing us at least a little closer to a possible generalization. We think of this toy model as a blueprint for other topological ferroic switching phenomena.

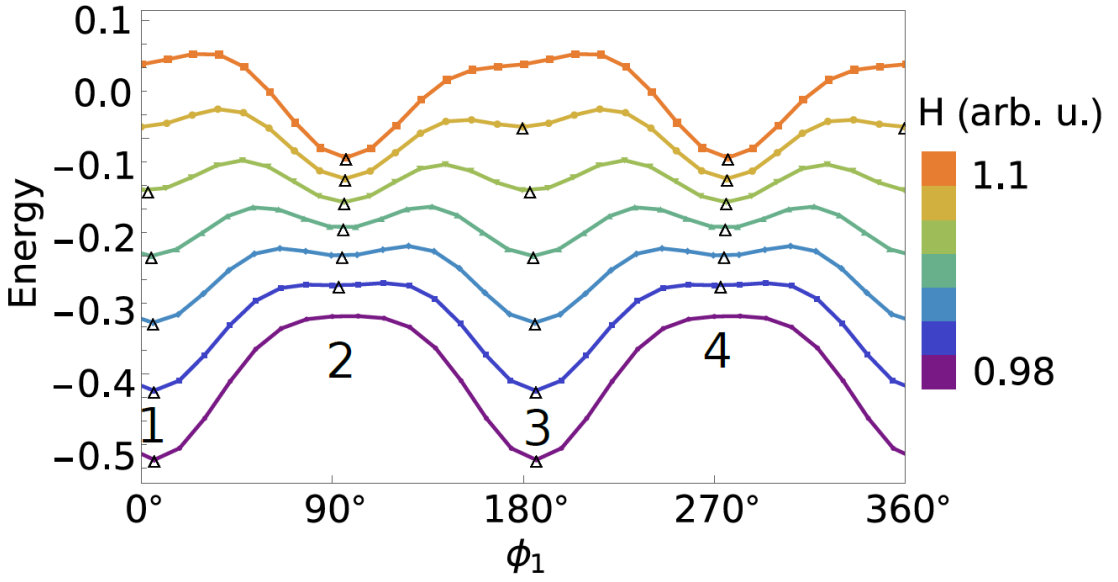

FIGURE 5.1: **PES barrier evolution** illustrating the topological switching between the four possible states of the system. PES color encodes the magnetic field strength. As the field is swept up and down, the state of the material is tracking the energy minimum, traced by triangles. Model parameters are $\gamma = 0.076$, $K_2 = -1$, $K_4 = -0.01$, $\beta = 5 * 10^{-5}$, $\alpha = 0.155$, $\phi_H = +8°$, H is ramped between 0.98 and 1.1 (arb. u.).

5.2 Electric control of magnetism

A natural consequence of constructing the model was then to consider the interaction not just with an external magnetic field but also with an external electric field:

$$F = \gamma(\mathbf{L}_1 \cdot \mathbf{L}_2)^2 - \alpha E_b \mathbf{L}_1 \cdot \mathbf{L}_2 \quad + \\ + \sum_{i=1,2} \left(k_2 \left(\mathbf{L}_i \cdot \mathbf{n}_i\right)^2 + k_4 (\mathbf{L}_i \cdot \mathbf{n}_i)^4 + (\mathbf{L}_i \cdot \mathbf{H})^2 + \beta L_{ix} L_{iy} H_x H_y \right) \tag{5.3}$$

This curiosity arises naturally not only from a desire for more comprehensive theory and theoretical and phenomenological model completeness but also from the fact that, on a technological level, applying the electric field is much more manageable, further increasing the hope for effective and innovative technology.

The electric control of magnetism was achived only in a handful of single-phase multiferroics, e.g. $BiFeO_3$, orthoferrites and hexaferrites Giovannetti and van den Brink, 2008; Ponet et al., 2022; Zhai et al., 2017. Usually, the low magnetically-induced electric polarization does not allow to change spin states with an applied electric field. Even in $GdMn_2O_5$ with one of the highest polarizations, $P = 3.5 \times 10^3\ \mu C \cdot m^{-2}$, measured in type-II multiferroics, the magnetoelectric energy for $E = 5 \times 10^4\ V \cdot cm^{-}1$ is about an order of magnitude smaller than the magnetic anisotropy energy and 2-3 orders of

magnitude lower than the exchange energy. In this paper, we demonstrate the electric control of magnetism in $GdMn_2O_5$ and discuss unique properties of this material, as well as general ingredients that can enable electrical spin manipulation in multiferroics.

Three factors make the electric control of magnetism in $GdMn_2O_5$ possible: (i) proximity to spin-flop transition, (ii) magnetic frustration and (iii) the relatively high magnetically-induced electric polarization. Near the flop transition, an effective magnetic anisotropy becomes small. The two kinds of antiferromagnetic chains in $GdMn_2O_5$ lead to two different flop transitions: (1) the Néel vectors $\mathbf{L}_1$ and $\mathbf{L}_2$ rotate in the same direction, in which case the electric polarization does not change and (2) they rotate in opposite directions, resulting in the sign change of the polarization. Importantly, opposite parities of $\mathbf{L}_1$ and $\mathbf{L}_2$ preclude linear coupling between the two order parameters and frustrate interchain interactions. At the same time, the electric polarization strongly depends on the angle between $\mathbf{L}_1$ and $\mathbf{L}_2$, which makes it possible to toggle magnetic states with an applied electric field.

The collaboration with Prof. Dr. Pimenov's group (Institut für Festkörperphysik, TU Wien, Austria) was vital, as it gave substance to the assumptions, observing the real physics, and allowing us to further test our model and the insights it suggested. The crucial role of an external electric field applied to our system allowed us to observe how the switching across the system's four states is achievable even outside the narrow angle region. Our model already suggested that at different values of the external magnetic field, and for different system parameters, the possible magic angle regions could vary. What was not yet clear is that, with the help of an external electric field, these ranges can be significantly shifted or reduced (depending on the intensity of the electric field), making the limitation of the narrow magic angle region something adjustable according to necessity and situation, and most importantly lifting stringent requirements for a precise orientation of the external magnetic field.

This is the key element that makes the entire concept highly appealing from a technological standpoint: an electric control of magnetism, achieving switching between the system states simply through an electric field, drastically reducing the need for a magnetic field with certain strength and oriented at a precise angle, which would be significantly more complex than applying or switching on/off an electric field.

Inversion symmetry breaking is often a result of magnetic frustration that gives rise to unusual spin states and low-energy collective modes. It would be interesting to explore the electric control of magnetism in other multiferroics near spin-flop and spin-reorientation transitions.

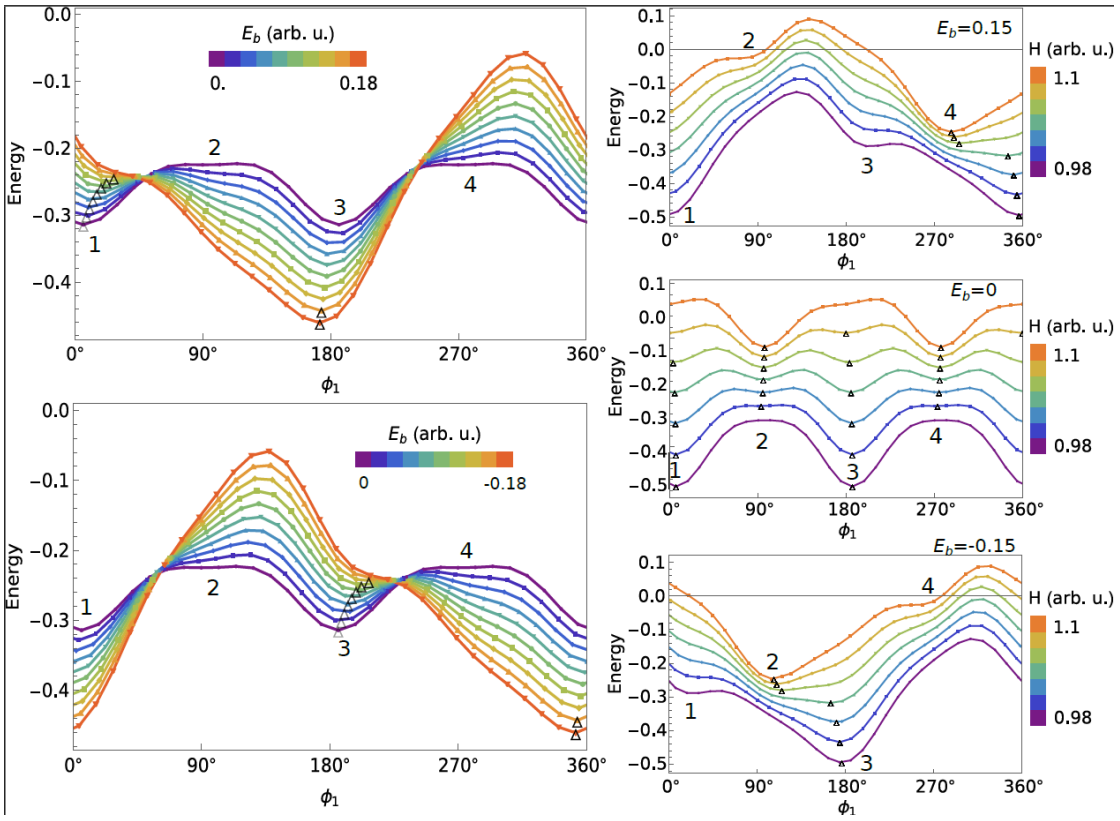

FIGURE 5.2: **Theoretical simulation of the effect of an external electric field**. Evolution of the barriers under an external electric field sweep, in the presence of a constant magnetic field oriented inside the magic angle region. Specific parameters and discussion are given in Chapter 4, Figure 4.1.

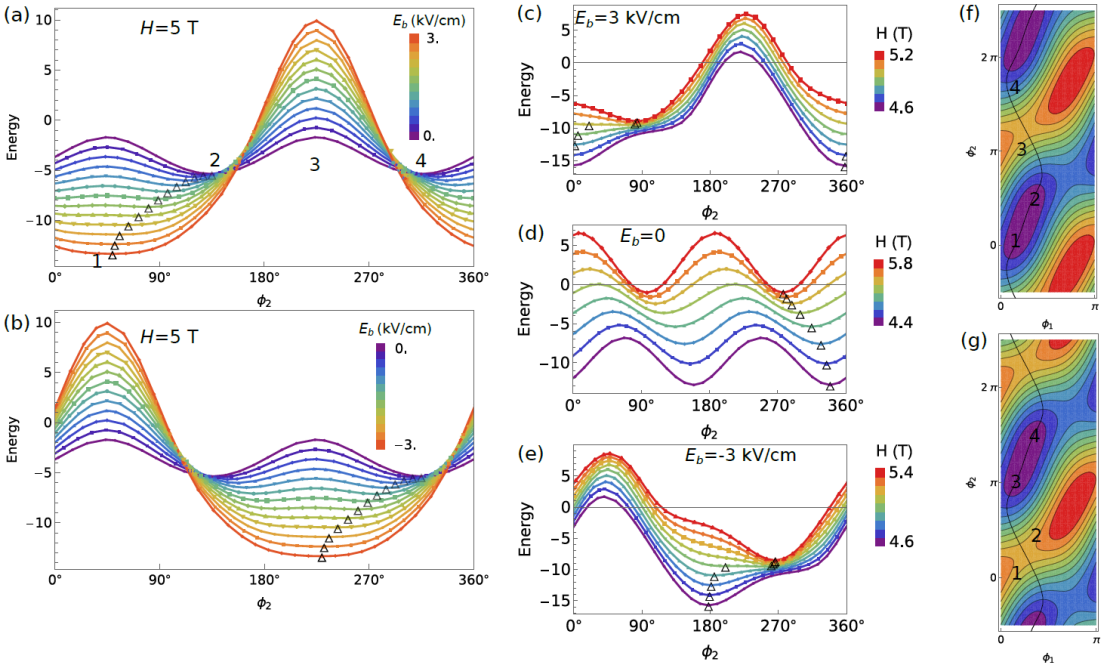

FIGURE 5.3: **Theoretical reproduction of PES evolution for a switching protocol realized in experiments**. Evolution of the barriers through an external electric field sweep, with a constant magnetic field oriented outside the magic angle region. Specific parameters and discussion are given in Chapter 4, Figure 4.6.

5.3 Final thoughts and future directions

The potential of this research is thus evident and so significant that one cannot settle for the few steps achieved, but the need naturally arises to study more deeply both this precise phenomenon and its more intimate reasons. The decisive role of an electric field can certainly be further explored but it undeniably seems to bring the possible technological application of this effect much closer. This calls with even greater urgency for an attempt to further generalize the model and create a tool that allows database screening in the hope of finding other materials that can give rise to this phenomenon, as well as identification of new classes of topological switching phenomena in ferroic materials, bringing even closer the applications and understanding of the physics involved.

Bibliography

Aroyo, M. I., Kirov, A., Capillas, C., Perez-Mato, J., & Wondratschek, H. (2006). Bilbao crystallographic server. ii. representations of crystallographic point groups and space groups. *Acta Crystallographica Section A: Foundations of Crystallography*, *62*(2), 115–128.

Aroyo, M. I., Perez-Mato, J. M., Capillas, C., Kroumova, E., Ivantchev, S., Madariaga, G., Kirov, A., & Wondratschek, H. (2006). Bilbao crystallographic server: I. databases and crystallographic computing programs. *Zeitschrift für Kristallographie-Crystalline Materials*, *221*(1), 15–27.

Bader, S. D. (2006). Colloquium: Opportunities in nanomagnetism. *Rev. Mod. Phys.*, *78*, 1–15. https://doi.org/10.1103/RevModPhys.78.1

Bibes, M., & Barthélémy, A. (2008). Towards a magnetoelectric memory. *Nature Materials*, *7*(6), 425–426. https://doi.org/10.1038/nmat2189

Campbell, B. J., Stokes, H. T., Tanner, D. E., & Hatch, D. M. (2006). Isodisplace: A web-based tool for exploring structural distortions. *Journal of Applied Crystallography*, *39*(4), 607–614.

Giovannetti, G., & van den Brink, J. (2008). Electronic correlations decimate the ferroelectric polarization of multiferroic $HoMn_2O_5$. *Phys. Rev. Lett.*, *100*, 227603. https://doi.org/10.1103/PhysRevLett.100.227603

Inc., W. R. (n.d.). Mathematica, Version 14.1 [Champaign, IL, 2024]. https://www.wolfram.com/mathematica

Mills, G., Jónsson, H., & Schenter, G. K. (1995). Reversible work transition state theory: Application to dissociative adsorption of hydrogen. *Surface Science*, *324*(2), 305–337. https://doi.org/https://doi.org/10.1016/0039-6028(94)00731-4

Nespolo, M. (2017). International tables for crystallography, volume a, space-group symmetry. edited by mois i. aroyo. wiley, 2016. pp. xxi+ 873. price gbp 295.00, eur 354.00 (hardcover). isbn 978-0-470-97423-0. *Acta Crystallographica Section A: Foundations and Advances*, *73*(3), 274–276.

Perez-Mato, J., Gallego, S., Tasci, E., Elcoro, L., de la Flor, G., & Aroyo, M. (2015). Symmetry-based computational tools for magnetic crystallography. *Annual Review of Materials Research*, *45*(Volume 45, 2015), 217–248. https://doi.org/https://doi.org/10.1146/annurev-matsci-070214-021008

Ponet, L., Artyukhin, S., Kain, T., Wettstein, J., Pimenov, A., Shuvaev, A., Wang, X., Cheong, S.-W., Mostovoy, M., & Pimenov, A. (2022). Topologically protected magnetoelectric switching in a multiferroic. *Nature*, *607*, 81–85. https://doi.org/10.1038/s41586-022-04851-6

Rice, M. J., & Mele, E. J. (1982). Elementary excitations of a linearly conjugated diatomic polymer. *Phys. Rev. Lett.*, *49*, 1455–1459. https://doi.org/10.1103/PhysRevLett.49.1455

Ryzhkov, M., Wettstein, J., Granero, A., Pimenov, A., Wang, X., Ponet, L., Cheong, S.-W., Mostovoy, M., Artyukhin, S., & Pimenov, A. (2024). Electric field control of multiple switching regimes in a multiferroic. *submitted*.

Stokes, H., Hatch, D., & Campbell, B. (2021). Isotropy software suite, iso. byu. edu. *There is no corresponding record for this reference*.

Thouless, D. J. (1983). Quantization of particle transport. *Phys. Rev. B*, *27*, 6083–6087. https://doi.org/10.1103/PhysRevB.27.6083

Weinan, E., Ren, W., & Vanden-Eijnden, E. (2002). String method for the study of rare events. *Physical Review B*, *66*(5), 052301.

Zhai, K., Wu, Y., Shen, S., Tian, W., Cao, H., Chai, Y., Chakoumakos, B. C., Shang, D., Yan, L., Wang, F., et al. (2017). Giant magnetoelectric effects achieved by tuning spin cone symmetry in y-type hexaferrites. *Nature communications*, *8*(1), 519.

Appendix A

Nudged Elastic Band method

The need for tracking the evolution of the minima, according to the transformation of the PES barriers following the variation of the external conditions, motivates the development of a method to study the minimum energy path (MEP), connecting two known stable configurations of the system's PES. It represents the lowest energy route the system traverses during its transition. It is essential to understand how a system can go from a state to another one. The two stable configurations mentioned usually represent the initial and final states of a transition, and particularly in our case they correspond to two local minima of the PES. For this purpose, the Nudged Elastic Band method (NEB) is a really powerful computational tool that is extensively used in condensed matter physics, as well as in theoretical chemistry, not only for understanding but also for quantifying processes like chemical reactions, molecular conformational changes and diffusion events in solids.
This method is usually implemented to overcome the drawbacks of other traditional methods, that usually fail very shortly. Such methods could be:

- Sequential descent methods:
  they begin at a local minimum on the potential energy surface and attempt to climb the energy landscape, following the path of slowest ascent, hoping to reach the saddle point (the highest energy point along the MEP). However, these methods often fail to identify the correct path, getting trapped in local minima or missing the saddle point entirely.

- Normal mode analysis:
  this method involves calculating the normal modes of vibration at a local minimum and then following each mode until a saddle point is found. This approach is limited to small systems and requires the computation of second derivatives of the potential energy surface, making it computationally demanding.

- Drag method:
  it involves defining a reaction coordinate, typically a linear interpolation between the initial and final configurations, and then minimizing the system energy with respect to all other degrees of freedom. While simple, this method often fails to identify the correct path, leading to discontinuous paths and missing the saddle point.

These standard methods are evidently limited, thus, when dealing with a complex potential energy surface, the need of a more versatile and robust technique arises. NEB method attempts to optimize this MEP search essentially by representing the transition path as a series of images (replicas) of the system. Each image corresponds to a specific point along the path, connected with neighbouring points by artificial springs to ensure a continuous and smooth path.
Its implementation can be summarized into the following steps:

1. Initialization
   NEB method begins requiring to specify the initial and final configurations of the system, which, usually, represent the initial and final states of the examined transition. They are the two ends of the chain, among which a set of intermediate evenly distributed images is generated. This images are connected between them by fictitious springs, forming indeed the elastic band.

2. Optimization
   The path is built according to the following conditions:

   - The physical force acting on each image should be perpendicular to the path, in order to avoid corner cutting when the path suddenly changes direction, keeping the images on the MEP.
   - The images should be evenly spaced along the path, and this should be achieved thanks to the spring forces acting along the NEB. Their purpose is to prevent the images from sliding down the PES, trying to accurately represent the MEP.
   - To ensure that the path is a true MEP and not just a local minimum, it is required for the images to be in a stable configuration. This means that the forces acting on them have to be minimized.

3. Nudging forces
   Two types of different forces are applied on each image:

- Physical forces, that are the real forces exerted by the PES on the atoms in the image. They are obtained from the potential energy function in this way:

$$F_i = -\nabla V(R_i)_\perp + F_{i_{||}} + f(\phi_i)\left(F_i - \nabla V(R_i)\cdot\tau_i\tau_i\right) \tag{A.1}$$

  Where τ_i is the unit vector representing the direction connecting two neighbouring images, defined as $\tau_i = \frac{R_{i+1}-R_{i-1}}{||R_{i+1}-R_{i-1}||}$; $V(R_i)$ is the energy potential in the position R_i of the i-th image; $-\nabla V(R_i)_\perp$ is the component of the physical force perpendicular to the path; $F_{i_{||}}$ is the component of the spring force that is parallel to the path; $f(\phi_i)$ is a switching function defined to be 1 if the angle between adjacent segments of the path is less than 90 degrees and 0 if the angle is greater than 90 degrees, used sometimes when it is implemented the correction to the perpendicular term of the force, that is $(f(\phi_i)\left(F_i - \nabla V(R_i)\cdot\tau_i\tau_i\right))$. This last term is not always implemented, since in some cases (as in the one of our interest) it is not necessary, as it will be clear in the picture showing our codes (for example in the third column of Figure 5.3 .

- The already mentioned fictitious spring forces, that maintain the connectivity and spacing between images. They act like springs pulling adjacent images towards each other, ensuring that the path is smooth and continuous

$$F_{i_{||}} = \left(k_{i+1}(R_{i+1} - R_i) - k_i(R_i - R_{i-1})\right)\tau_i \tag{A.2}$$

  where k_{i+1} and k_i are spring constants that determine the strength of the spring forces and R_{i+1}, R_i and R_{i-1} are the positions of the i-th image and its previous and following neighbours.

- The crucial step of the nudging is then ready to be implemented, involving two key projections to maintain the accuracy of the MEP. The first one has to project out the component of the spring force that is perpendicular to the path, to prevent the images from being pulled off the path by these forces. The second one has to project out the component of the physical force that is parallel to the path, to prevent images from sliding down the potential energy surface along the path.

4. Convergence

   This procedure is iterated continuously until the forces acting on all the images are minimized, resulting in the state where the images are in a stable configuration and the path formed is actually the minimum energy one. That is, the process involves a series of iterations where the positions are adjusted until they reach a stable equilibrium.

A.1 Climbing Image optimization

Even if this method is a great improvement with respect to traditional ones, it still struggles in certain situations, for example it cannot always identify the saddle points (that correspond to the physical transition states) of the PES. To overcome this problem, the Climbing Image optimization of the NEB method (CI-NEB) is introduced. Its main feature is indeed pinpointing the saddle points.
CI-NEB works in three main steps:

1. Identification
   After a first relaxation of the NEB images, one of the images is identified as the climbing image. This corresponds to the image with the highest potential energy along the path. This image is assumed to be closest to the saddle point.

2. Force modification
   Instead of applying the usual physical and spring forces to the climbing image, a modified force is applied:

$$F_{climb} = -\nabla V(R_i) + 2\nabla V(R_i) \cdot \tau_i \tau_i \tag{A.3}$$

   which is essentially the physical force, with the component parallel to the path changed in sign. While $-\nabla V(R_i)$ represents the physical force acting on the image, $2\nabla V(R_i) \cdot \tau_i \tau_i$ is a correction that reverses the component of the physical force parallel to the path, thus pushing the climbing images uphill towards the saddle points, this being the goal of this modified force.

3. Saddle point convergence
   The climbing images, only experiencing this modified force, do not feel any spring forces. This results in their convergence to the exact saddle points when the forces on them become zero. The climbing images indeed basically climb the potential energy surface until they reach the saddle points.

Hence, to summarize the benefits of this method, NEB method ensures a reliable and robust approach, capable of handling more complex scenarios than traditional methods can do. It can also be implemented with high efficiency, taking advantage of the fact that the computations for each image can be performed independently on parallel computers, bringing significant speedups (fundamental when considering large systems). This power comes yet with great flexibility and simplicity, making it useful and versatile for a wide range of research.

A.2 NEB method in our simulations

The following pictures show the codes where CI-NEB method by Mills et al., 1995; Weinan et al., 2002 has been implemented for our purpose. As it can be seen, we omit the switching function correction (third term eq. A.1). This is because the correction has been found unnecessary in our case, making it possible to keep the implementation even simpler.

In the grey box, Fig. A.1, fundamental quantities of the problem are defined, as well as it was done in Chapter 3. $\mathbf{L}_1$ and $\mathbf{L}_2$ are defined as unit vector, with ϕ_1 and ϕ_2 being the angles of their orientation with respect to the easy axes directions of chains 1 and 2, namely $\mathbf{n}_1$ and $\mathbf{n}_2$, which are also unit vectors and are initialized with angles of respectively +6° and -6° with respect to the a-axis. The external magnetic field H is also decomposed in its components along a-axis and b-axis, using its angle of orientation ϕ_H. In the green boxes (Fig. A.2, A.3, A.4, A.5), we show the actual implementation of the NEB method, with the Climbing Image optimization implemented in the second one.

Initialization of order parameters

```
L1 = {Cos[ϕ1], Sin[ϕ1]};
L2 = {Cos[ϕ2], Sin[ϕ2]};
n1 = {Cos[ϕ], Sin[ϕ]} /. ϕ → 6 * π / 180
n2 = {Cos[ϕ], Sin[ϕ]} /. ϕ → -6 * π / 180
Hvec = h {Cos[ϕh], Sin[ϕh]}
```

FIGURE A.1: Order parameters initialization

```
NEB[PES_, init12_, nImages_ : 30, init_ : {}] := Module[{dim, var, ends, images, τ, F, Fu, Fpar, Fperp, Ene, μ},
  dim = Length[init12[[1]]];
  var = Array[Subscript[x, #] &, {dim}];
  ends = FindMinimum[PES @@ var, Sequence[{var, #}ᵀ]][[2, All, 2]] & /@ init12;
  images = If[init == {}, Table[(1 - x) ends[[1]] + x ends[[2]], {x, 0, 1, 1 / nImages}], init];
  τ[i_] := Normalize[images[[i + 1]] - images[[i - 1]]];
  (*200 steps along the force, or until the force is below the tolerance (0.01)*)
  Do[
   F = Table[
     Fu = - (Grad[PES @@ var, var] /. Thread[var → images[[j]]]);

     Fperp = (IdentityMatrix[dim] - τ[j]⊗τ[j]).Fu;
     μ = 1;
     While[PES @@ (images[[j]] + μ Fperp) > PES @@ (images[[j]]), μ /= 2];
     Fperp *= μ;
     Fperp + (τ[j]⊗τ[j]).(images[[j + 1]] + images[[j - 1]] - 2 images[[j]])
     , {j, 2, Length[images] - 1}];
   (*for each image, simplified line search;
   if step 0.5 leads to overshoot (energy grows), divide the step by two*)
   (*images[[2;;-2]]+=0.5F;*)(*overshoots when the gradienients are large*)
   Do[
    μ = 1;
    While[PES @@ (images[[i]] + μ F[[i - 1]]) > PES @@ (images[[i]]), μ /= 2];
    images[[i]] += μ F[[i - 1]];
    , {i, 2, Length[images] - 1}];
   If[Norm[Flatten[F]] < 0.001, Break[]];
   , {step, 10}];
```

FIGURE A.2: Defining NEB method

```
(*climbing images -- positions the images above neighbors at the maxima*)
Do[
 Ene = PES @@@ images;
 F = Table[
   Fu = - (Grad[PES @@ var, var] /. Thread[var → images[[i]]]);
   Fperp = (IdentityMatrix[dim] - τ[i]⊗τ[i]).Fu;
   Fpar = (τ[i]⊗τ[i]).Fu;


   μ = 0.005;
   While[PES @@ (images[[i]] + μ Fpar) > PES @@ (images[[i]]), μ /= 2];
   Fpar *= μ;

   μ = 0.005;
   While[PES @@ (images[[i]] + μ Fperp) > PES @@ (images[[i]]), μ /= 2];
   Fperp *= μ;

   If[(Ene[[i]] > Ene[[i - 1]]) && (Ene[[i]] > Ene[[i + 1]]),

    (*we climb along the band to the top of the potential*)
    Fperp - Fpar,

    If[(Ene[[i]] < Ene[[i - 1]]) && (Ene[[i]] < Ene[[i + 1]]),
     (*we climb down along the band to the bottom of the potential*)
     Fperp + Fpar,

     (*we move along the band to equilibrate the distances*)
     Fperp + μ (τ[i]⊗τ[i]).(images[[i + 1]] + images[[i - 1]] - 2 images[[i]])
    ]]
   , {i, 2, Length[images] - 1}];

 images[[2 ;; -2]] += F;

 If[Norm[Flatten[F]] < 0.001, (*Print[step];*)Break[]];
 , {step, 20 000}];

{images, PES @@@ images}]
```

FIGURE A.3: Climbing image optimization applied at our NEB method

A.2.1 Optimization using second derivatives

In order to reduce the arbitrariness of the step size and its variation intrinsic to the basic NEB method, and most of all with the purpose of getting more precise shifts of the images at each optimization step, we implemented a second derivative correction. The use of second derivatives is usually avoided in NEB implementation, since they are not accessible analytically for complex energy surfaces, and estimating them numerically would lead to enormous amount of calculations. Also, using second derivatives in step estimation near inflection points or away from a local minimum is counterproductive and does not improve the convergence. Nevertheless, close to the minimum, where the function is represented as $f = \frac{1}{2}x^T Ax + bx$, using the Hessian matrix $A_{ij} = \partial^2 f / \partial x_i \partial x_j$

gives a reliable step size $\delta x = -A^{-1}b$ and that step size can be heuristically used to estimate the step size along the entire NEB. In our codes with such an implementation we have seen a big improvement in stability and convergence speed, allowing us to get considerably more precise NEB bands in fewer iterations.

```
NEB[PES_, init12_, nImages_ : 30, init_ : {}] := Module[{dim, var, ends, images, τ, F, Fu, Fpar, Fperp, Ene, μ, d2},
  dim = Length[init12[[1]]];
  var = Array[Subscript[x, #] &, {dim}];
  ends = FindMinimum[PES @@ var, Sequence[{var, #}ᵀ]][[2, All, 2]] & /@ init12;
  d2 = Max[Table[Eigenvalues[Grad[Grad[PES @@ var, var], var] /. Thread[var → p]], {p, ends}]];
  If[init == {},
   images = Table[(1 - x) ends[[1]] + x ends[[2]], {x, 0, 1, 1 / nImages}],
   images = init; images[[{1, -1}]] = ends];
  τ[i_] := Normalize[images[[i + 1]] - images[[i - 1]]];
  (*200 steps along the force, or until the force is below the tolerance (0.01)*)
  Do[
   F = Table[
     Fu = - (Grad[PES @@ var, var] /. Thread[var → images[[j]]]);

     Fperp = (IdentityMatrix[dim] - τ[j] ⊗ τ[j]).Fu / (2 d2); (*d2 is the correction from second derivative*)
     μ = 1;
     While[PES @@ (images[[j]] + μ Fperp) > PES @@ (images[[j]]), μ /= 2];
     Fperp *= μ;
     Fperp + (τ[j] ⊗ τ[j]).(images[[j + 1]] + images[[j - 1]] - 2 images[[j]])
     , {j, 2, Length[images] - 1}];
   (*for each image, simplified line search;
   if step 0.5 leads to overshoot (energy grows), divide the step by two*)
   (*images[[2;;-2]]+=0.5F;*)(*overshoots when the gradienients are large*)
   Do[
    μ = 1;
    While[PES @@ (images[[i]] + μ F[[i - 1]]) > PES @@ (images[[i]]), μ /= 2];
    images[[i]] += μ F[[i - 1]];
    , {i, 2, Length[images] - 1}];
   If[Norm[Flatten[F]] < 0.0001, Break[]];
   , {step, 10}];
```

FIGURE A.4: Implementation of second derivative correction in NEB method

```
(*climbing images -- positions the images above neighbors at the maxima*)
Do[
 Ene = PES @@@ images;
 F = Table[
   Fu = -(Grad[PES @@ var, var] /. Thread[var → images[[i]]]);
   Fperp = (IdentityMatrix[dim] - τ[i]⊗τ[i]).Fu;
   Fpar = (τ[i]⊗τ[i]).Fu;


   μ = 0.005;
   While[PES @@ (images[[i]] + μ Fpar) > PES @@ (images[[i]]), μ /= 2];
   Fpar *= μ;

   μ = 0.005;
   While[PES @@ (images[[i]] + μ Fperp) > PES @@ (images[[i]]), μ /= 2];
   Fperp *= μ;

   If[(Ene[[i]] > Ene[[i - 1]]) && (Ene[[i]] > Ene[[i + 1]]),

    (*we climb along the band to the top of the potential*)
    Fperp - Fpar,

    If[(Ene[[i]] < Ene[[i - 1]]) && (Ene[[i]] < Ene[[i + 1]]),
     (*we climb down along the band to the bottom of the potential*)
     Fperp + Fpar,

     (*we move along the band to equilibrate the distances*)
     Fperp + μ (τ[i]⊗τ[i]).(images[[i + 1]] + images[[i - 1]] - 2 images[[i]])
    ]]
   , {i, 2, Length[images] - 1}];

 images[[2 ;; -2]] += F;

 If[Norm[Flatten[F]] < 0.001, (*Print[step];*)Break[]];
 , {step, 20000}];

{images, PES @@@ images}]
```

FIGURE A.5: Once the second derivative is implemented in the first part, there is no need to correct the Climbing Image optimization, which remains the same as before

A.2.2 Implementation of NEB method for computing the evolution of the system

Blue boxes in Figure A.6 present the tools for computing NEB bands to visualize the Potential Energy Surface, as described in Chapters 3 and 4, evolving due to the sweeps of the external magnetic field in a certain range, and with a fixed external electric field. PES parameters can be specified according to necessities. The last box makes possible to plot the bands evolution as needed, while the previous one is used to manually fix singular bands in case of minor divergences. Pink boxes in Figure A.7 are completely analogue to the blue ones in Fig. A.6, but with inverted roles for the external magnetic and electric fields. The combination of what showed in Figures A.6 and A.7 enable to produce plots like the ones illustrated for examples in Figure 5.2 or 5.3. Finally, yellow boxes in Figure A.8 compute and then plot phase diagram for polarization behaviour with respect to

ϕ_1 and ϕ_2 during magnetic field sweeps within a certain range of intensities and with different value of fixed electric fields (like the ones displayed in Figure 4.5. Also in here, PES parameters respect same necessities and choice criteria as in the codes discussed above.

Sweeping H field

```
hsNEB = Table[hval, {hval, 4.6, 5.4, 0.1}]
nebs = ParallelTable[
   PES[ϕ1_, ϕ2_] = (K2 ((L1.n1)^2 + (L2.n2)^2) + g (L1.L2)^2 + K4 ((L1.n1)^4 + (L2.n2)^4) + ((L1.Hvec)^2 + (L2.Hvec)^2) + β (L1[[1]] × L1[[2]] + L2[[1]] × L2[[2]]) Hvec[[1]] × Hvec[[2]] - α Eb L1.L2 /.
      {K4 → -0.01 * 25, K2 → -1 * 25, g → 25 * 0.076, ϕh → -4 * π / 180, h → hval, Eb → -2, α → 0.155 * 25, β → 125*^-5});
   {ang, bar} = NEB[PES, {{0.6, -0.7}, {0.6, 2 π - 0.7}}, 30];
   {Join[{#1 - 2 π, #2 - 2 π} & @@@ ang, ang, {#1 + 2 π, #2 + 2 π} & @@@ ang], Join[bar, bar, bar]}, {hval, hsNEB}];

hs = Flatten@Table[{hsNEB, Reverse@hsNEB}, {2}];
min = {0, {ϕ1 → 0.4, ϕ2 → 2 π}};
sweep = Table[
   PES[ϕ1_, ϕ2_] = (K2 ((L1.n1)^2 + (L2.n2)^2) + g (L1.L2)^2 + K4 ((L1.n1)^4 + (L2.n2)^4) + ((L1.Hvec)^2 + (L2.Hvec)^2) + β (L1[[1]] × L1[[2]] + L2[[1]] × L2[[2]]) Hvec[[1]] × Hvec[[2]] - α Eb L1.L2 /.
      {K4 → -0.01 * 25, K2 → -1 * 25, g → 25 * 0.076, ϕh → -4 * π / 180, h → hval, Eb → -2, α → 0.155 * 25, β → 125*^-5});
   min = FindMinimum[PES[ϕ1, ϕ2], {{ϕ1, ϕ1 /. min[[2]]}, {ϕ2, ϕ2 /. min[[2]]}}];
   {ϕ1, Mod[ϕ2, 2 π], PES [ϕ1, ϕ2]} /. min[[2]], {hval, hs}];

Table[nfrom = n - 1;
  nebs[n] = Table[
     PES[ϕ1_, ϕ2_] = (K2 ((L1.n1)^2 + (L2.n2)^2) + g (L1.L2)^2 + K4 ((L1.n1)^4 + (L2.n2)^4) + ((L1.Hvec)^2 + (L2.Hvec)^2) + β (L1[[1]] × L1[[2]] + L2[[1]] × L2[[2]]) Hvec[[1]] × Hvec[[2]] - α Eb L1.L2 /.
        {K4 → -0.01 * 25, K2 → -1 * 25, g → 25 * 0.076, ϕh → -4 * π / 180, h → hval, Eb → 0, α → 0.155 * 25, β → 125*^-5});
     {ang, bar} = NEB[PES, {nebs[nfrom, 1, 1], nebs[nfrom, 1, 1] + {0, 2 π}}, 30, Partition[nebs[nfrom, 1], Length[nebs[1, 1]] / 3][[2]]];
     {Join[{#1 - 2 π, #2 - 2 π} & @@@ ang, ang, {#1 + 2 π, #2 + 2 π} & @@@ ang], Join[bar, bar, bar]}, {hval, {hs[n]})}][[1]], {n, {3}}];

ListPlot[Table[{nebs[hi, 1, All, 2], nebs[hi, 2]}^T, {hi, Length@nebs}], Joined → True, PlotMarkers → {Automatic, Tiny}, Frame → True, FrameLabel → {"ϕ2", "Energy"},
 LabelStyle → {16, Black}, PlotStyle → ColorData["Rainbow"] /@ Range[0, 1, 1 / (Length@nebs - 1)], PlotRange → {{0, 2 π}, All},
 FrameTicks → {{Automatic, None}, {{#, ToString[180 # / π] <> "°"} & /@ (π Range[0, 2, 1 / 2]), None}},
 PlotLegends → Placed[SwatchLegend[hs, LegendLayout → {"Column", 1}, LegendLabel → "H (T)"], Right],
 Epilog → {Table[{PointSize[Medium], Text[Style["△", 16], {#2, #3}] & (*Point*) @@ sweep[hi]}, {hi, Length@nebs}]}, ImageSize → Medium]
```

FIGURE A.6: Computation of the evolution of the PES with magnetic field using NEB, and simulations of magnetic field sweeps.

Sweeping E field

```
es = Table[ebval, {ebval, 0, -3, -0.25}];
nebs = ParallelTable[
   PES[ϕ1_, ϕ2_] = (K2 ((L1.n1)^2 + (L2.n2)^2) + g (L1.L2)^2 + K4 ((L1.n1)^4 + (L2.n2)^4) + ((L1.Hvec)^2 + (L2.Hvec)^2) + β (L1[[1]] × L1[[2]] + L2[[1]] × L2[[2]]) Hvec[[1]] × Hvec[[2]] - α Eb L1.L2 /.
      {K4 → -0.01 * 25, K2 → -1 * 25, g → 25 * 0.076, ϕh → -4 * π / 180, h → 5, Eb → ebval, α → 0.155 * 25, β → 125*^-5});
   {ang, bar} = NEB[PES, {{0.7, -1.4}, {0.7, -1.4 + 2 π}}, 30];
   {Join[{#1 - 2 π, #2 - 2 π} & @@@ ang, ang, {#1 + 2 π, #2 + 2 π} & @@@ ang], Join[bar, bar, bar]}, {ebval, es}];

min = {0, {ϕ1 → 0.7, ϕ2 → 6}};
sweep = Table[
  PES[ϕ1_, ϕ2_] = (K2 ((L1.n1)^2 + (L2.n2)^2) + g (L1.L2)^2 + K4 ((L1.n1)^4 + (L2.n2)^4) + ((L1.Hvec)^2 + (L2.Hvec)^2) + β (L1[[1]] × L1[[2]] + L2[[1]] × L2[[2]]) Hvec[[1]] × Hvec[[2]] - α Eb L1.L2 /.
     {K4 → -0.01 * 25, K2 → -1 * 25, g → 25 * 0.076, ϕh → -4 * π / 180, h → 5, Eb → ebval, α → 0.155 * 25, β → 125*^-5});
  min = FindMinimum[PES[ϕ1, ϕ2], {{ϕ1, ϕ1 /. min[[2]]}, {ϕ2, ϕ2 /. min[[2]]}}];
  {ϕ1, ϕ2, PES [ϕ1, ϕ2]} /. min[[2]], {ebval, es}]

Table[nebs[n] = Table[
     PES[ϕ1_, ϕ2_] = (K2 ((L1.n1)^2 + (L2.n2)^2) + g (L1.L2)^2 + K4 ((L1.n1)^4 + (L2.n2)^4) + ((L1.Hvec)^2 + (L2.Hvec)^2) + β (L1[[1]] × L1[[2]] + L2[[1]] × L2[[2]]) Hvec[[1]] × Hvec[[2]] - Eb L1.L2 /.
        {K4 → -0.01 * 25, K2 → -1 * 25, g → 25 * 0.076, ϕh → -4 * π / 180, h → 5, Eb → ebval, α → 0.155 * 25, β → 125*^-5});
     {ang, bar} = NEB[PES, {{2.1, -0.8}, {2 π + 2.1, -0.8}}, 30, Partition[nebs[n - 1, 1], Length[nebs[1, 1]] / 3][[2]]];
     {Join[{#1 - 2 π, #2} & @@@ ang, ang, {#1 + 2 π, #2} & @@@ ang], Join[bar, bar, bar]}, {ebval, {es[n]})}][[1]], {n, {6}}];

ListPlot[Table[{nebs[hi, 1, All, 2], nebs[hi, 2]}^T, {hi, Length@nebs}], Joined → True, PlotMarkers → {Automatic, Tiny}, Frame → True, FrameLabel → {"ϕ2", "Energy"},
 LabelStyle → {14, Black}, PlotStyle → ColorData["Rainbow"] /@ Range[0, 1, 1 / Length@nebs], PlotRange → {{0, 2 π}, All},
 FrameTicks → {{Automatic, None}, {{#, ToString[180 # / π] <> "°"} & /@ (π Range[0, 2, 1 / 2]), None}},
 PlotLegends → Placed[SwatchLegend[es, LegendLayout → {"Column", 1}, LegendLabel → "Eb (arb. u.)"], Right], ImageSize → 500,
 Epilog → {Table[{PointSize[Medium], Text[Style["△", {16, Bold, Opacity[Rescale[hi, {0, Length@nebs}, {0.3, 1}]]}], sweep[hi, {2, 3}]]}, {hi, Length@nebs}]},
 Axes → False]
```

FIGURE A.7: Computation of the evolution of the PES with electric field using NEB, and simulations of electric field sweeps.

Polarization Phase Diagrams

```
hs = 5 Flatten@Table[Join[Table[hval, {hval, 0.9, 1.3, 0.01}], Reverse@Table[hval, {hval, 0.9, 1.3, 0.01}]], {4}];
sweepAngles = ParallelTable[
   min = {0, {ϕ1 → -0.7, ϕ2 → -0.8}};
   Table[
    PES[ϕ1_, ϕ2_] = (K2 ((L1.n1)^2 + (L2.n2)^2) + g (L1.L2)^2 + K4 ((L1.n1)^4 + (L2.n2)^4) + ((L1.Hvec)^2 + (L2.Hvec)^2) + β (L1[[1]] × L1[[2]] + L2[[1]] × L2[[2]]) Hvec[[1]] × Hvec[[2]] - α Eb L1.L2 /.
        {K4 → 30 * -0.01 * 25, K2 → -1. * 25, g → 3 * 25 * 0.076, ϕh → fH, h → hval, Eb → +2, α → 0.155 * 25, β → 125*^-5}) / 25;
    min = Quiet@FindMinimum[PES[ϕ1, ϕ2], {{ϕ1, ϕ1 /. min[[2]]}, {ϕ2, ϕ2 /. min[[2]]}}, Method → {"Newton", "StepControl" → {"TrustRegion", "MaxScaledStepSize" → .5}}],
    {hval, hs}], {fH, 0, maxfH = 2 π / 20, stepfH = π / 360 / 8}];

ListDensityPlot[Cos[ϕ1 - ϕ2] /. sweepAngles[All, All, 2]', PlotRange → {-1, 1}, DataRange → {{0, maxfH}, {0, 1}},
 FrameTicks → {{{#, 5 Abs@Chop[2 ArcSin[Sin[2 π #]] / π]} & /@ Range[0, 1, 0.25 / 2], None}, {Range[0, maxfH, 3 * 16 stepfH],
    {#, ToString[180 / π * #] <> "°"} & /@ Range[0, maxfH, 64 stepfH]}}, InterpolationOrder → 0, PlotLegends → BarLegend[Automatic, LegendLabel → Subscript[P, b]],
 ColorFunction → "TemperatureMap", LabelStyle → {Black, 14}, FrameLabel → {"ϕh", "H"}, GridLines → {{7.8 π / 180}, None}]
```

FIGURE A.8: Computation and plotting of polarization switching history during H field sweeps for different field orientations.